Article

The Impact of Upstream Static Deformation on Flow Past a Cylinder/Flare

Aaron Becks [ID], Tyler Korenyi-Both, Jack J. McNamara * and Datta V. Gaitonde [ID]

Department of Mechanical and Aerospace Engineering, The Ohio State University, Columbus, OH 43210-1276, USA; becks.16@osu.edu (A.B.); korenyi-both.1@buckeyemail.osu.edu (T.K.-B.); gaitonde.3@osu.edu (D.V.G.)
* Correspondence: mcnamara.190@osu.edu

Abstract: Reynolds-averaged Navier–Stokes simulations are performed for supersonic turbulent flow over a cylinder/flare with upstream surface distortion representative of structural deformation induced via fluid–structural and fluid–thermal–structural behavior. Broad parametric analysis is carried out through the generation of Kriging-response surfaces from a database of general simulations. A posteriori simulations are then carried out at parametric combinations that correspond to extrema in the Kriging response surfaces to gain deeper insights into the interaction between the surface distortion and flow responses. Upstream distortions tend to decrease, rather than increase, the peak pressure and heat flux loads on the flare compared to an undeformed cylinder. Furthermore, decreases in these quantities reach up to $O(10\%)$ compared to up to $O(1\%)$ for increases. Integrated quantities over the flare are relatively insensitive to upstream distortion. The corner separation length is the most sensitive quantity to upstream distortion, with protrusions tending to increase the separation length and recessions reducing the separation length. Modifications in the separation length of up to 40% are observed. Reductions in peak loads tend to correspond to increases in the corner separation length. The movement of the surface distortion relative to the corner indicates a negligible impact beyond 1.5 distortion lengths from the corner, and the largest impact on the corner separation length occurs when distortion is directly adjacent. These results are an important step toward understanding and quantifying the impact of surface deformations on downstream components.

Keywords: fluid–structure interactions (FSIs); Reynolds-averaged Navier–Stokes (RANS); surrogate modeling; Kriging

1. Introduction and Problem Statement

The impact of deformed surfaces, due to aerothermoelastic behavior, on downstream components is a key area of study in high-speed vehicle development [1–6]. Locally, deforming surfaces perturb the boundary layer through induced pressure gradients, including shocks and expansion fans, which can either instigate or modify local flow separation [7,8]. The impact of such surface deformations on downstream components is currently not well understood. The goal of this paper is to explore the effects of canonical surface deformations and develop a parametric model for surface loads. For concreteness, a cylinder/flare configuration at supersonic turbulent flow conditions is considered.

A large body of recent research has investigated fluid–structure interactions (FSI) in high-speed flow [8–24]. However, most prior work has primarily focused on local impacts on the flowfield, with an emphasis on dynamic aeroelastic effects. Downstream effects are generally ignored. Two noteworthy sets of observations highlight the difficulty in assessing downstream effects. A study by Beberniss et al. [5] detected frequencies corresponding to structural motion in the pressure spectra downstream of a shock–boundary layer interaction (SBLI) over a compliant surface. However, a similar study by Peltier et al. [6] could not replicate this downstream effect of panel compliance. The root cause of the discrepancy was unclear, and it remains uncharacterized.

Static aeroelastic behaviors, like passive control bumps, are also pertinent to the downstream response [25–29]. These bumps help manage SBLI separation or modify the boundary layer characteristics to enhance downstream-component performance. Evidence also suggests that mean static deformations may have more lasting effects on turbulent boundary layers than dynamic deformations [30]. Additionally, both intentional modifications and unintentional structural changes, including permanent deformations and damaged panels, can significantly affect downstream components [4,30].

In the present study, a cylinder/flare platform [31–39] was selected. The presence of corner flow, and the associated separation, arising in this and related configurations, such as a double cone, adds the necessary complexity that exists in slender high-speed vehicles. Despite the attention given to flare geometries, studies on fluid–structural interactions within this context remain relatively sparse, though recent studies analyzing FSI phenomena embedded on a ramp [18,19] and upstream of a ramp [40,41] indicate an emerging consideration of this configuration for FSI research.

This paper seeks to characterize the impact of upstream surface distortions, characteristic of mean aerothermoelastic deformations typically seen in thermally or mechanically buckled thin-gauge skin panels, on downstream components. To this end, Reynolds-averaged Navier–Stokes (RANS) simulations were performed and benchmarked against experimental data and then incorporated into surrogate models using Kriging to develop trend-level studies via broad parametric analysis. Key parametric combinations of interest are identified and studied in detail using a posteriori RANS simulations.

2. Methodology

2.1. Problem Description

A representation of the cylinder/flare configuration and a corresponding mesh are shown in Figure 1. Different surface distortions were introduced upstream of the flare corner to generate various flow perturbations whose impact on the corner flow separation and attendant fluid response over the flare surface could be studied. Examples of the types of surface distortions implemented in this work are found in Figure 2, defined as convex or protrusions, concave or recessions, combined convex–concave or protrusion–recession, vice versa, and general deformations.
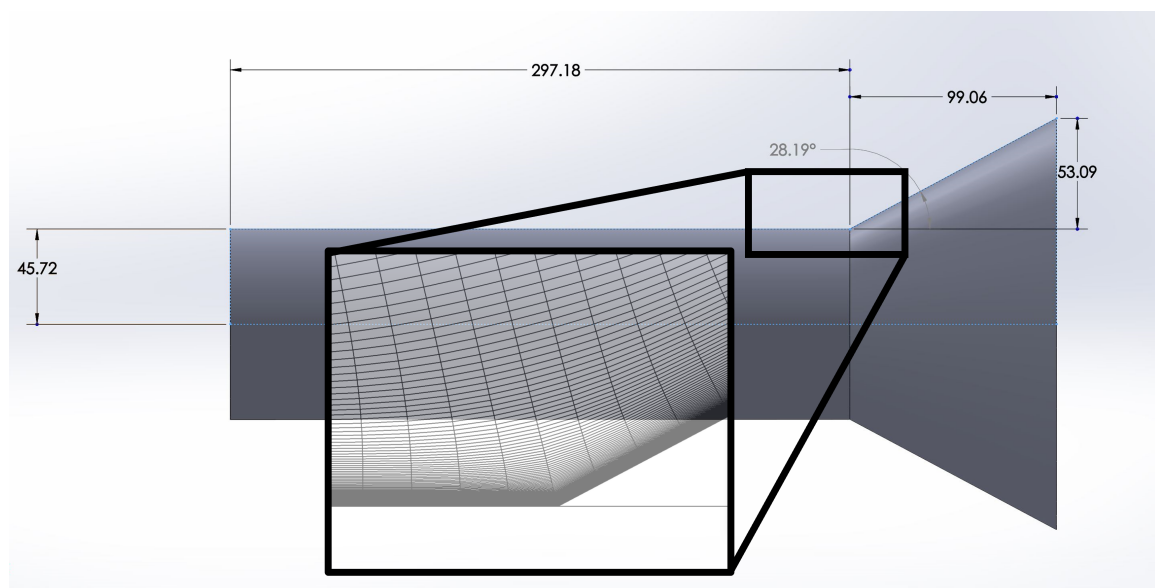

Figure 1. Cylinder/flare configuration (dimensions in millimeters and degrees).
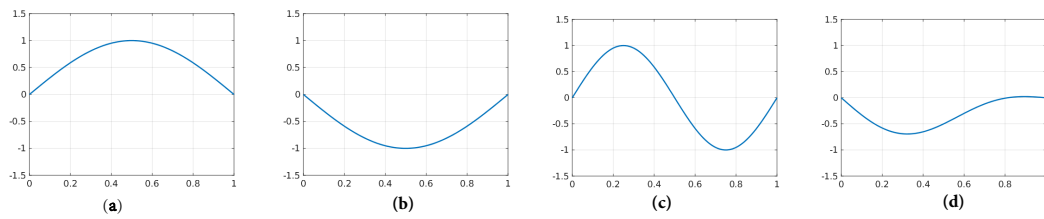
Figure 2. Deformation example nomenclature. (**a**) Positive mode 1, $A_1 = 1$, $A_2 = 0$, convex/protrusion. (**b**) Negative mode 1, $A_1 = -1$, $A_2 = 0$, concave/recession. (**c**) Positive mode 2, $A_1 = 0$, $A_2 = 1$, convex–concave/protrusion–recession. (**d**) General deformation, $A_1 = -0.5$, $A_2 = -0.3$, mostly concave/recessed.

The computational domain is an axisymmetric plane set above the axisymmetric cylinder/flare. The wall of the cylinder/flare is set to a no-slip, isothermal condition at a temperature of 300 K (room temperature). The computational domain is set to be the same as the experimental domain identified by Chism [42,43], where the cylinder body does not have a leading nose body. Therefore, the left boundary is set to a constant, uniform inlet boundary, and the boundary layer is allowed to grow naturally. The top and right boundaries are set to far-field extrapolation.

The flow and overall distortion parameters were chosen to emulate experimental conditions from Section 2.3, and they are listed in Tables 1 and 2. The distortions introduced upstream of the cylinder/flare were developed using mode shapes corresponding to a pinned–pinned 1D panel configuration:

$$\delta_v(x) = \sum_{i=1}^{m} A_i \sin\left(\frac{i\pi x}{L}\right) \tag{1}$$

where A_i is the peak amplitude of the corresponding mode number, i is the mode number of the distortion, L is the length of the distortion, and m is the total desired number of mode shapes of the distortion. Surface distortions spanning modes 1 and 2 were considered, i.e., $m = 2$. The distortion length was kept constant at $L = 58$ mm, while A_1 and A_2 are the modal amplitude parameters that are varied according to Table 2. Distortions are set in the cylinder at variable distances from the flare corner, where the distance from the flare to the end of the distortion, in panel lengths, is ℓ. The distances span from zero panel lengths from the flare (abutting the corner) to the end of the distortion ($\ell = 0$) to two panel lengths from the flare to the end of the distortion ($\ell = 2$).

Table 1. Constant simulation inputs.

Variable	Value
M_∞	7
Re (1/m)	1.3×10^5
T_∞ (K)	51
Distortion length, L (mm)	58

Table 2. Simulation input parameters

Lower Limit	Variable	Upper Limit
0	Distance from flare, ℓ (panel lengths)	2
-3.3	Amplitude mode 1, A_1 (mm)	3.3
-2.2	Amplitude mode 2, A_1 (mm)	2.2

2.2. Fluid Dynamics Model

Flow predictions were generated using the compressible Reynolds-averaged Navier–Stokes (RANS) solutions through the DOD CREATE AV CFD software (version 12.8.1) Kestrel [44–47]. The solution method uses a second-order spatial scheme and a second-order Newton time integration scheme with advective temporal damping and three subiterations. Steady-state solutions were obtained with a starting Courant–Friedrichs–Lewy (CFL) number of 100, ramped to 1000. Grid selection considerations and convergence results are presented in Appendix A.1, while an iterative residual convergence assessment is provided in Appendix A.2. For all simulations, the turbulence intensity at the inlet and freestream was set to 0.1, and the eddy viscosity ratio was set to 0.01.

2.3. Companion Experimental Configurations and Comparisons

The simulation parameters are modeled after representative experiments conducted at the University of Tennessee Space Institute (UTSI) Mach 7 wind tunnel, which is a Ludwieg tube with a free jet test section. A detailed description and characterization of the tunnel are available from Gragston et al. [48]. Various deformed cylinder and cylinder/flare experiments were tested [42,43] at the flow conditions listed in Table 3.

Table 3. Simulation/experiment parameters.

M_∞	Re (1/m)	p_0 (Pa)	T_0 (K)	p_∞ (Pa)	T_∞ (K)	T_w (K)	ρ_∞ (kg/m^3)	u_∞ (m/s)
7.0	1.3×10^5	1.07×10^6	560	257.8	51.9	300	0.0173	1010

Since adiabatic wall temperatures are difficult to measure experimentally [42], for simplicity, a modified Stanton number using total temperature, T_0, was used instead of adiabatic wall temperature, T_{aw}. The modified Stanton number is defined in Equation (2), and it is compared to RANS predictions in Figure 3. The value $x = 0$ corresponds to the location of the flare corner. In the simulations, two turbulence closure models were considered: the Spalart–Allmaras (SA) model and the Menter–Shear Stress Transport (SST) model. Although all models display an increase in heat transfer near the same location ($x = 0$, the flare corner), the downstream predictions show significant differences. The SA model tends to underrepresent the peak Stanton number and subsequent decay. In contrast, the SST model aligns more closely with the experimental results on the flare wall, more accurately predicting the peak value location and magnitude. Based on this assessment, the Menter–SST model is used for turbulence closure in the remainder of this paper.

$$St = \frac{q}{c_p \rho_\infty u_\infty (T_0 - T_w)} \tag{2}$$

Schlieren visualizations from the experiments, including those for an undeformed cylinder/flare and a convex, positive mode 1 shape ($A_1 = 3$ mm, $A_2 = 0$ mm) positioned 1-panel length upstream of the flare ($\ell = 1$), were compared with the simulation results. The experimental and numerical schlieren results are displayed in Figure 4. Figure 4a,b shows experimental schlieren results from Chism [42], and Figure 4c,d depicts these same results but darkened to show the low contrast in shock densities compared to the low densities within the tunnel. In all cases, the shock waves due to the flow turn at the flare corner were about 34 to 35 degrees. The shock angles between the experimental and simulated data deviated by one degree or less, corresponding to an error of less than 3%. Furthermore, the shock given off the wall distortions was both 12 degrees. These results indicate the suitability of the RANS simulations for the present purposes with this configuration and flow conditions for the trend-level analysis to follow.
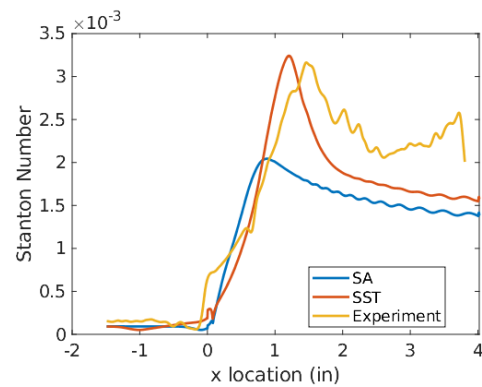
Figure 3. Experimental comparison of Stanton number to RANS simulations with turbulence model comparisons. Flare corner located at x = 0.
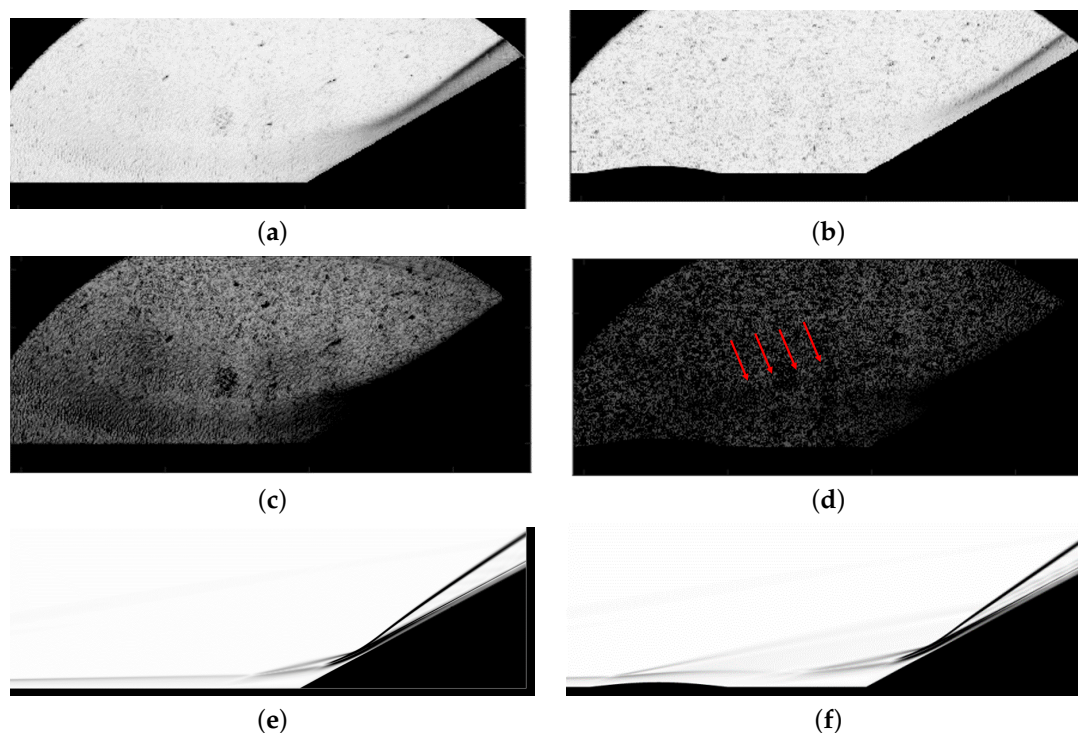

Figure 4. Experimental and simulated schlieren comparisons for the undeformed and deformed (mode 1) surfaces. (**a**) Experimental schlieren in the Mach 7 tunnel, undeformed. (**b**) Experimental schlieren in the Mach 7 tunnel, convex, positive mode 1 configuration ($A_1 = 3$). (**c**) Experimental schlieren darkened to see contrast, undeformed. (**d**) Experimental schlieren darkened to see contrast, convex, positive mode 1 configuration ($A_1 = 3$). Arrows point to the shock given off the deformation. (**e**) RANS schlieren in the Mach 7 cylinder/flare configuration, undeformed. (**f**) RANS schlieren in the Mach 7 cylinder/flare configuration, convex, positive mode 1 ($A_1 = 3$).

2.4. Surrogate Modeling

Even though RANS simulations are relatively more economical compared to scale-resolving approaches, a full factorial study of the parameter space using RANS simulations represents a significant computational expense. The present work addresses this challenge through a surrogate-based approach. Surrogates emulate CFD simulations within defined input domains [49–51], and have proven successful in emulating steady CFD predictions across a variety of complex flow fields [23,24,52–57]. Among such methods, Kriging models represent a relatively simple, efficient, and effective method for generating surrogate models, and they were selected for use in the current study [49,58,59].

A Halton sequence [60] was implemented using SciPy [61], an open-source Python library, to generate low-discrepancy and quasi-random input parameters. This method was chosen since it provides flexibility to adapt the number of samples throughout the study and also guarantees better space-filling characteristics in lower dimensions [60]. The bounds considered for the operating conditions parameter space are listed in Table 4.

Table 4. Kriging model inputs, ℓ, A_1, A_2.

Lower Limit	Variable	Upper Limit
0	Distance from flare, ℓ (panel lengths)	2
-3.3	Amplitude mode 1, A_1 (mm)	3.3
-2.2	Amplitude mode 2, A_1 (mm)	2.2

An important consideration when generating Kriging surrogates for flow responses is the potential for linked parameters. [62] This occurs when the flow indirectly responds to the input parameters through a linked equation, such as the total distortion in Equation (1). In such cases, the generality of the surrogate model is degraded if the sampling of the input parameters is carried out naively in an independent manner [62]. The use of hyperellipsoid sampling ensures a consistent and uniform sampling over the total distortion amplitude (Equation (1)), as described by Grier et al. [62].

The development of the surrogate models closely followed the process outlined by Korenyi-Both [59]. Insights into the history, applications, derivation, and algorithms of Kriging models were detailed by Krige [63], Matheron [64], Korenyi-Both [59], and Rasmussen and Nickisch [65]. The overarching framework for crafting a surrogate model is depicted in Figure 5. The process is as follows:

1. Determine the input–output relationship: First, the correlation between the input and output must be established. For this study, the modal amplitudes of distortions and the location relative to the flare corner served as input parameters, and the pressure, heat flux, and skin friction coefficient profiles were the output functions.
2. Define the sample space: The next step was to identify a sampling method (for example, Sobol or Halton sequence) and sample space that comprehensively spans the desired input parameters.
3. Generate training data: Training data were then generated using the database of RANS solutions discussed in Section 2.2.
4. Construct a surrogate model: After the training data were collated, the Kriging surrogate model was generated, as described in Appendix B.
5. Prediction using the trained model: Response surfaces were constructed using the Kriging model to fill in the space between RANS simulations and develop a trend analysis.

The Kriging models in this work were developed and implemented with the SciKit-Learn package in Python [66], and they used SciPy [61] optimization methods. Two hundred RANS CFD cases were generated to train and validate the surrogate model, spanning the parameter space using a Halton sequence. The kernel selection is among the most important factors in model performance [65,67]; thus, four kernel architectures were considered in this study: Radial Basis Function (RBF), Matern, WhiteKernel, and ConstantKernel. The details of each kernel can be found in the work of Duvenaud [67]. Additionally, several combinations of these four kernels were tested; 80% of the data, randomly selected, were reserved for training, 10% for model testing, and the remaining 10% for final validation. The selection and convergence of the models are discussed in Appendix B.
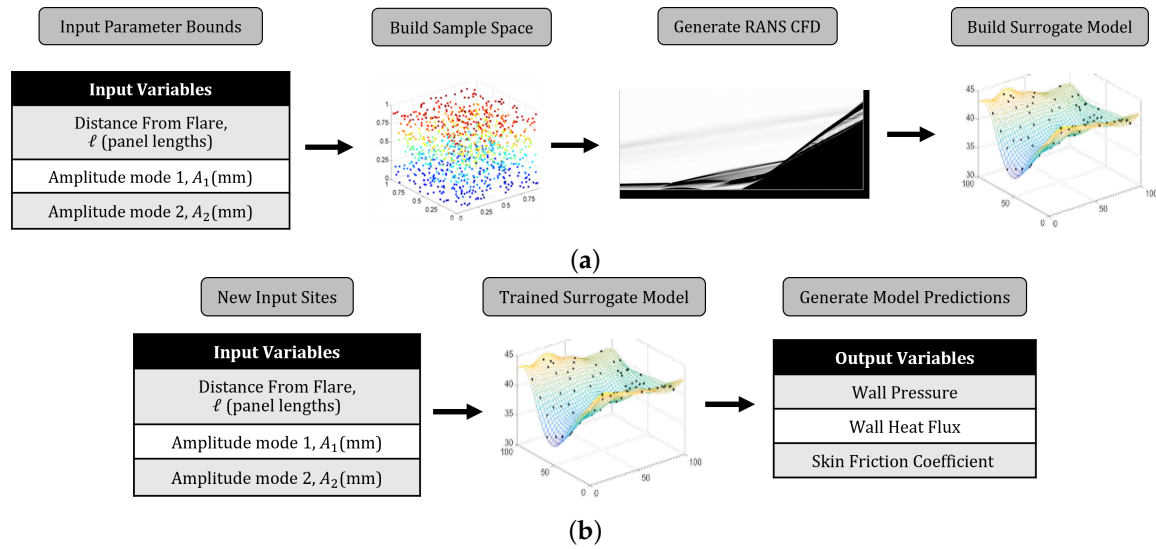
(a)

(b)

Figure 5. Workflow in generating surrogate models and response surfaces. (**a**) Building surrogate model. (**b**) Using surrogate model.

3. Results

Trend analysis was carried out using Kriging response surfaces with a focus on the peak and integral values of the pressure, heat flux, and corner separation length. The interactions of the distortion with the corner separation, as well as the downstream influence and persistence of upstream perturbations, were explored. Key distortion shapes and locations were studied in depth using a posteriori RANS simulations at identified input parameter combinations to elucidate the underlying physical mechanisms.

3.1. Impact of Distortion Shape

A Kriging surrogate model was developed, designed with only the modal amplitude contributions (A_1 and A_2) as variables. In this case, the distance from the flare of the distortion was set to a constant value of one panel length ($\ell = 1$). Thus, the downstream effects of distortion shape and size were isolated. The Kriging model for this study, defined in Equation (3), with details on the selection and generation in Appendix B.1, was used to generate pressure, heat flux, and skin friction profiles over the span of the input parameter space (Table 5); examples of these profiles are found in Appendix B.1. The peak values of the pressure and heat flux profiles on the flare, as well as the integral of the pressure and heat flux over the flare, and the separation length at the flare corner for the Kriging model predictions are shown in Figures 6–10. The Kriging prediction for the maximal value in these figures is denoted with a star, while the minimal values are denoted with stars and numbers. A posteriori RANS simulations were conducted at parametric combinations of modal amplitudes that corresponded to the maximal and minimal values from the Kriging response surfaces for each quantity.

Table 5. Kriging model inputs, A_1 and A_2.

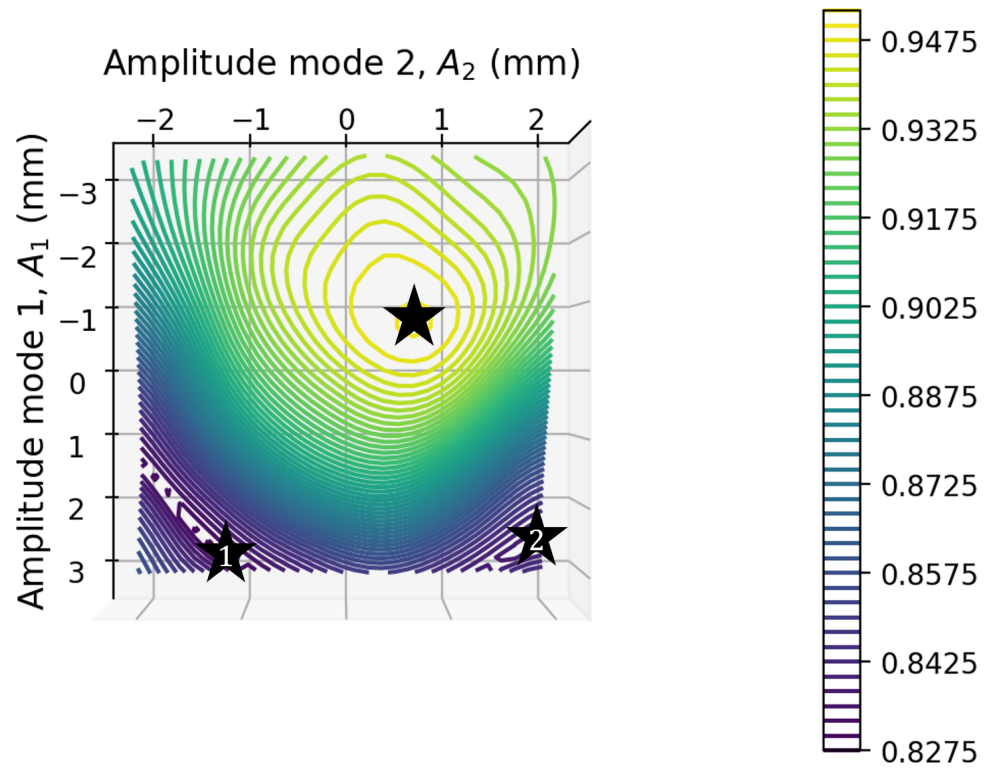| Lower Limit	Variable	Upper Limit
-3.3	Amplitude mode 1, A_1 (mm)	3.3
-2.2	Amplitude mode 2, A_1 (mm)	2.2

Figure 6. Kriging model pressure peaks (psi), varying A_1 and A_2. The unmarked star represents the maximal pressure peak, and the numbered stars represent the 2 minimal pressure peaks.
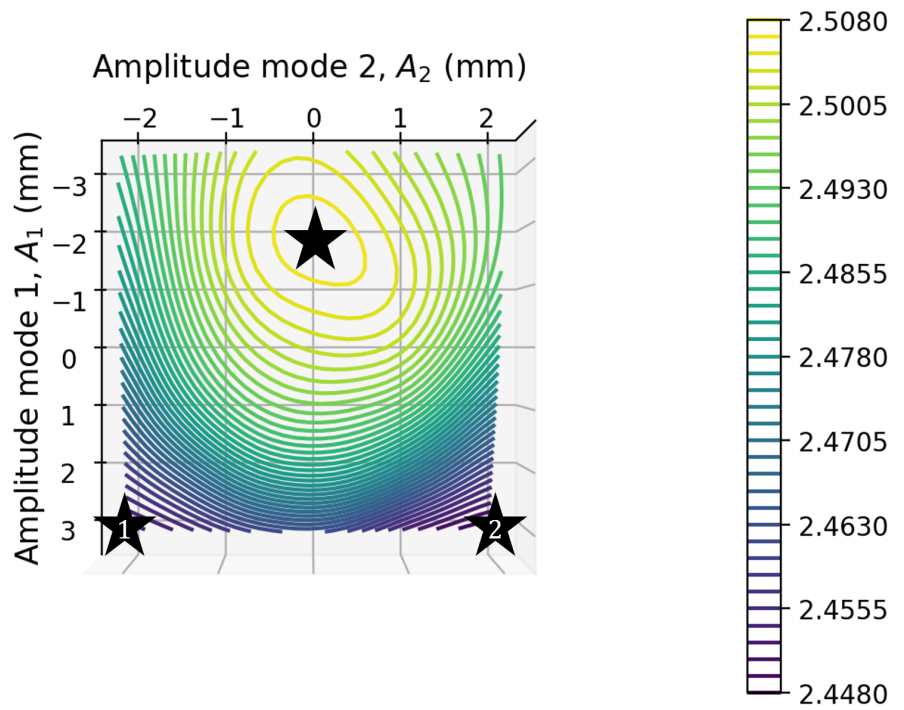

Figure 7. Kriging model pressure integral (psi-in), varying A_1 and A_2. The unmarked star represents the maximal pressure integral, and the numbered stars represent the 2 minimal pressure integral.
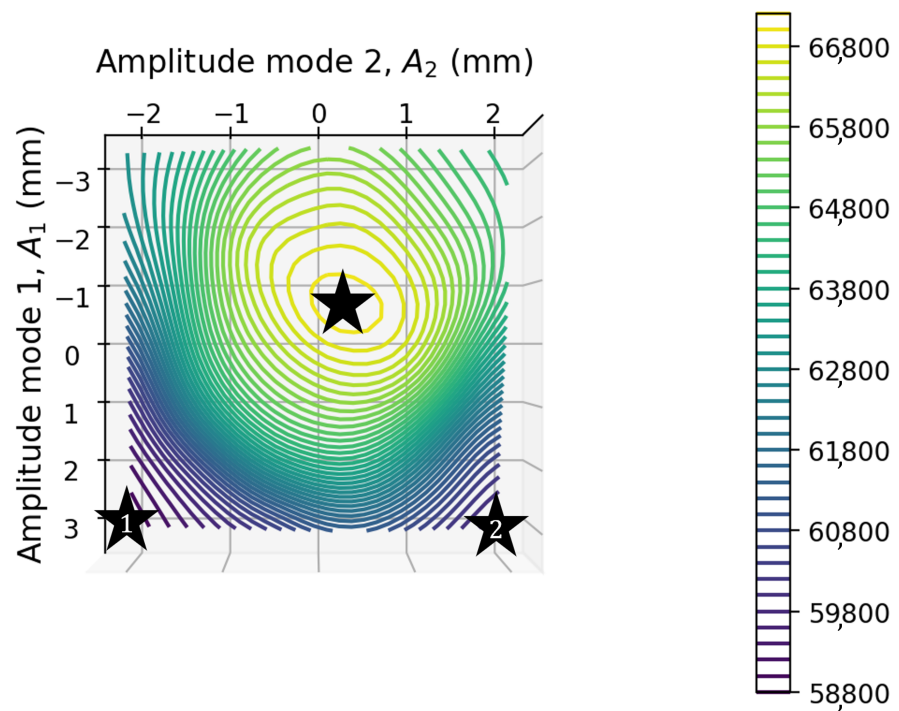
Figure 8. Kriging model heat flux peaks, (W/m^2), varying A_1 and A_2. The unmarked star represents the maximal heat flux peak, and the numbered stars represent the 2 minimal heat flux peaks.
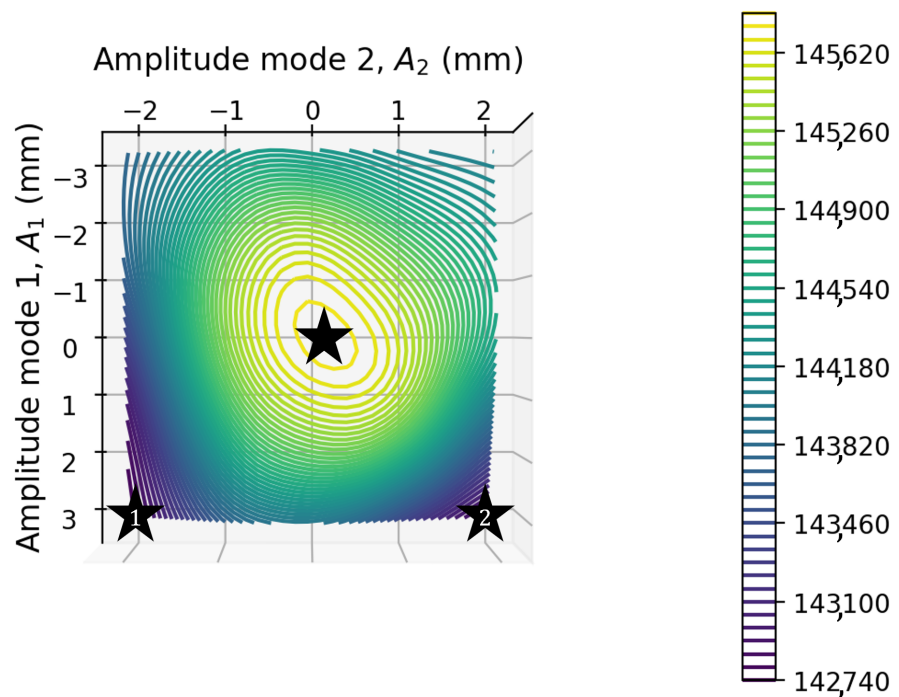

Figure 9. Kriging model heat flux integral, $(W/m^2 - in)$, varying A_1 and A_2. The unmarked star represents the maximal heat flux integral, and the numbered stars represent the 2 minimal heat flux integral.
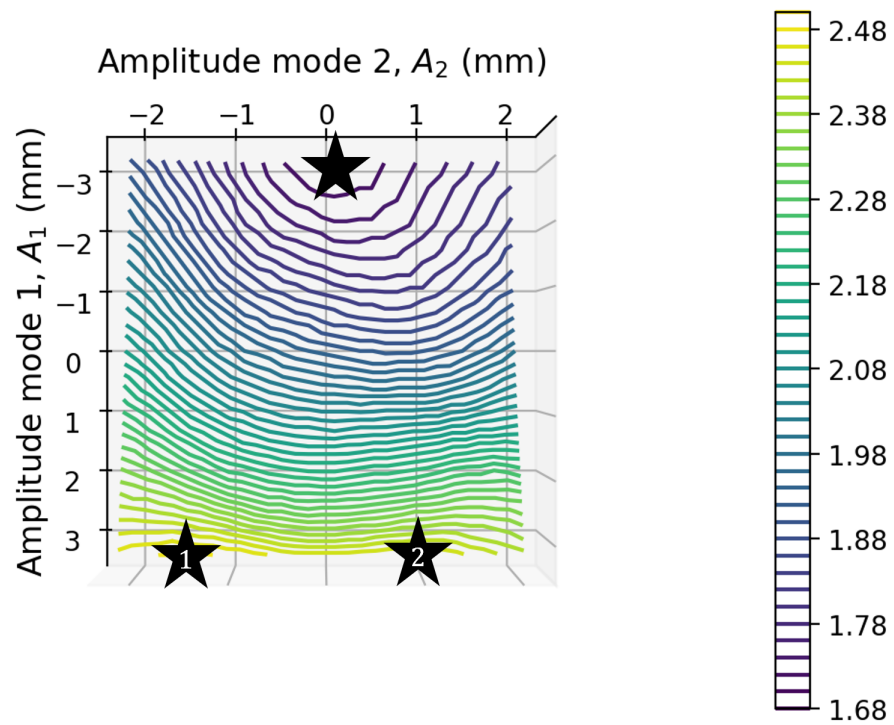
Figure 10. Kriging model separation length (in), varying A_1 and A_2. The unmarked star represents the minimum separation length, and the numbered stars represent the 2 maximum separation lengths.

The maximal and minimal values and modal contributions from both the Kriging and the subsequent RANS simulations, as well as the percentage differences from the undeformed case, are listed in Tables 6–10. Compression/expansion contours depicting the shock structure of the flow response are shown in Figure 11, while the streamlines of the separation corner variations are shown in Figure 12. For the former, $\vec{v} \cdot \nabla p$, was used, which takes positive values at adverse pressure gradients (shocks) and negative values for expansions, and contours of pressure greater than 0.8 psi are overlaid in pink. For the latter, streamlines are displayed to visualize corner separation/recirculation bubbles, and contours of temperature greater than 445 K are overlaid in pink. Finally, pressure and heat flux profiles on the cylinder/flare are shown in Figures 13 and 14, generated using RANS simulations of distortions that were identified to cause maximal and minimal integrated pressure and heat flux via the Kriging model

$$0.000342 + 6.656 \cdot Matern(lengthscale = 4.2, \nu = 1.5) + WhiteKernel(noiselevel = 0.103) \tag{3}$$

Table 6. Peak pressure maxima and minima predictions.

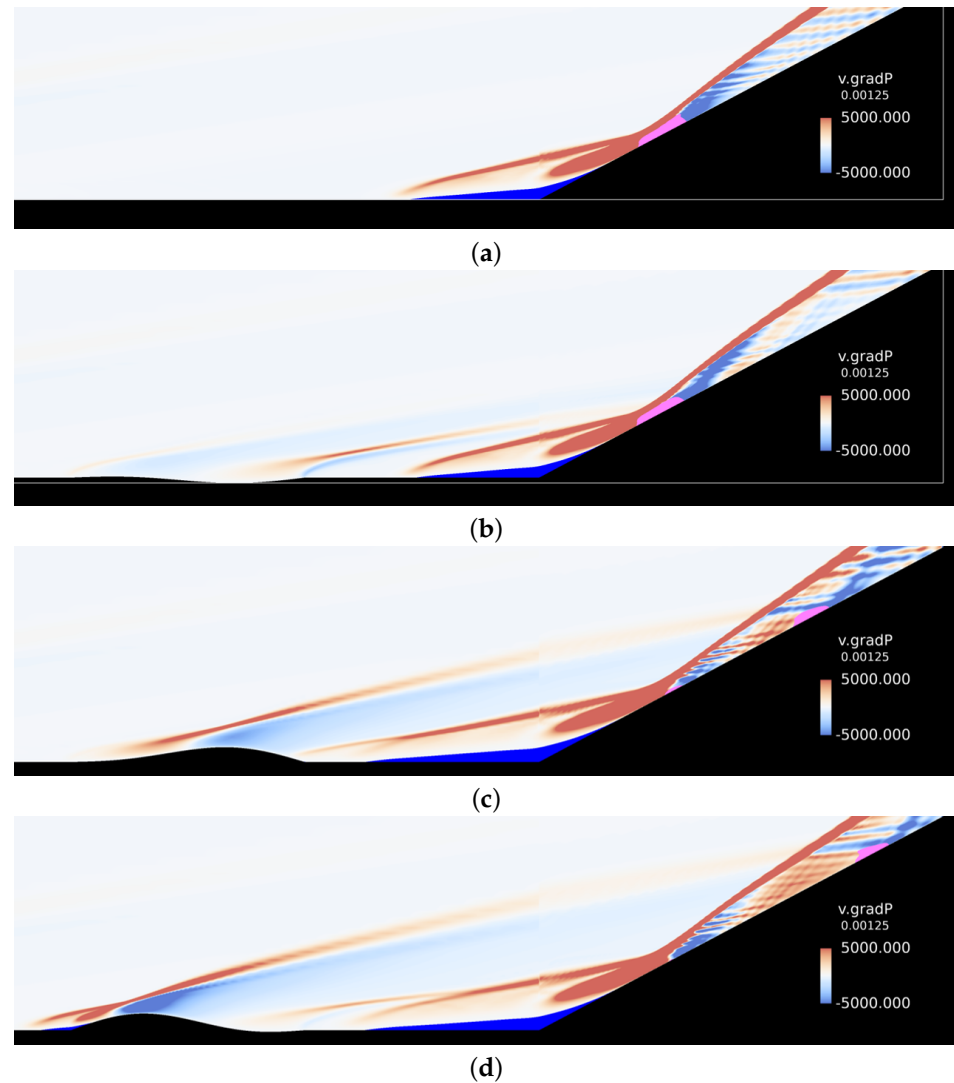|	Kriging Prediction		RANS Prediction	
Configuration	Pressure Peak (psi)	% Difference from Flat	Pressure Peak (psi)	% Difference from Flat
Flat, $A_1 = 0$, $A_2 = 0$	0.9403	N/A	0.9403	N/A
Max Pressure Peak Case, $A_1 = -0.756$, $A_2 = 0.735$	0.9488	+0.91%	0.9488	+0.91%
Min Pressure Peak Case 1, $A_1 = 2.914$, $A_2 = -1.262$	0.8298	−11.8%	0.8179	−13%
Min Pressure Peak Case 2, $A_1 = 2.699$, $A_2 = 2.018$	0.8343	−11.3%	0.8148	−13.3%

Figure 11. Shock structure of the maxima and minima pressure peak cases, shown as $\vec{v} \cdot \nabla p$. Expansions are shown in blue (negative) and compressions in red (positive). Corner separation ($u < 0$) is overlaid in dark blue, and near-peak pressures (greater than 0.8 psi) are overlaid in pink. (**a**) Flat, $A_1 = 0$, $A_2 = 0$. (**b**) Maxima pressure peak case, $A_1 = -0.756$, $A_2 = 0.735$. (**c**) Minima pressure peak case 1, $A_1 = 2.914$, $A_2 = -1.262$. (**d**) Minima pressure peak case 2, $A_1 = 2.699$, $A_2 = 2.018$.

The predicted peak pressure values of the Kriging model as a function of the input distortion amplitudes are shown in Figure 6. A narrow band of upstream surface distortions led to increases in the peak surface pressure, albeit only marginally ($\sim$1%). Generally, the introduction of upstream distortions decreased the peak pressure, with maximum reductions for the bounds considered of up to 12%. Furthermore, it is evident that the introduction of upstream distortion tends to reduce the pressure peak by up to 12%.

A comparison of the Kriging and RANS pressure peak predictions for the extrema conditions is listed in Table 6. The Kriging model predictions captured the peak pressure values to a 2% difference from the RANS predictions. The RANS-predicted shock structures generated via these distortions are shown in Figure 11. The pressure gradient associated with the flare–corner shock induced corner separation. The initial flow turn after separation resulted in a separation shock; in the nominal flat case, the peak pressure occurred where the separated shear layer and separation shock impinged on the flare. Distortions introduced an additional set of waves. These altered the pattern observed in the undeformed case, and they modified both the peak value and the width of the pressure profile. In Figure 11b, the maximal pressure peak case occurs when a strong distortion-induced compression

wave impinges directly at the separation-induced shock impingement location. Conversely, the pressure peak minima case occurs when a strong expansion wave impinges near the separation-induced shock impingement location, reducing the peak pressure value, as seen in Figure 11c,d. The compression waves from the front half of the distortion in these cases impinged further downstream, introducing additional peaks similar in magnitude to the separation-induced shock-impingement peak.

Table 7. Maxima and minima pressure integral predictions.

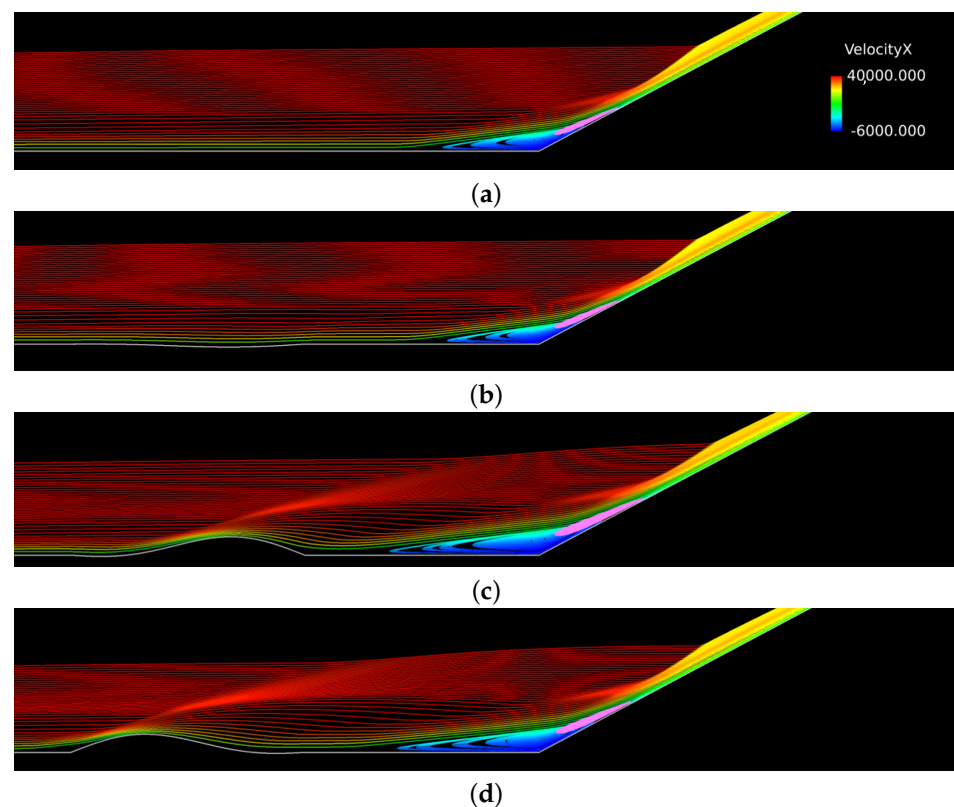|	Kriging Prediction		RANS Prediction	
Configuration	**Pressure Integral over Flare (psi-in)**	**% Difference from Flat**	**Pressure Integral over Flare (psi-in)**	**% Difference from Flat**
Flat, $A_1 = 0$, $A_2 = 0$	2.502	N/A	2.502	N/A
Max Pressure Integral Case, $A_1 = -1.620$, $A_2 = 0.0$	2.507	+0.19%	2.507	+0.19%
Min Pressure Integral Case 1, $A_1 = 2.914$, $A_2 = -1.262$	2.452	−2.0%	2.416	−3.5%
Min Pressure Integral Case 2, $A_1 = 2.699$, $A_2 = 2.018$	2.448	−2.2%	2.414	−3.5%

(a)

(b)

(c)

(d)

Figure 12. Streamlines of the maximal and minimal heat flux peak cases. Note the corner separation in the blue recirculation bubble. The peak off-body temperature (greater than 445 K) is overlaid in a pink contour. (**a**) Flat, $A_1 = 0$, $A_2 = 0$. (**b**) Maxima heat flux peak case, $A_1 = -0.540$, $A_2 = 0.307$. (**c**) Minima heat flux peak case 1, $A_1 = 3.131$, $A_2 = -2.118$. (**d**) Minima heat flux peak case 2, $A_1 = 3.131$, $A_2 = 2.018$.

The model-predicted pressure integrated over the flare is shown in Figure 7. The upper and lower bounds of the integrated pressure were predicted to vary by about 2%,

indicating that the impact of upstream distortion on the pressure was muted in an integral sense compared to the peak pressure.

A comparison between the Kriging- and RANS-predicted pressure integrals, presented in Table 7, showed a less-than-2% difference in the modeled value from the RANS result. Pressure profiles of the RANS simulations at the Kriging model predicted integral maxima and minima, as shown in Figure 13. The pressure profile for the maximal pressure integral case exhibited a widening of the peak pressure, which was caused by the distortion-induced shock impingement near this location. Conversely, when the pressure integral minima occurred, the primary pressure peaks were reduced due to the impingement of expansion waves; however, secondary peaks occurred downstream due to the impingement of compression waves given off of the distortions. This redistribution of the peak value led to only minor differences in the total integrated pressure on the flare compared to the undeformed cylinder configuration.

The Kriging response surface for peak heat flux is shown in Figure 8. The upper and lower bounds varied by 12% of the maximum value. In this case, the maximal peak heat flux was located near the undeformed state. This indicates that almost any perturbation to the boundary layer in this upstream region augments the boundary layer and recirculation corner to reduce the relative peak off-body temperature and wall heat flux.
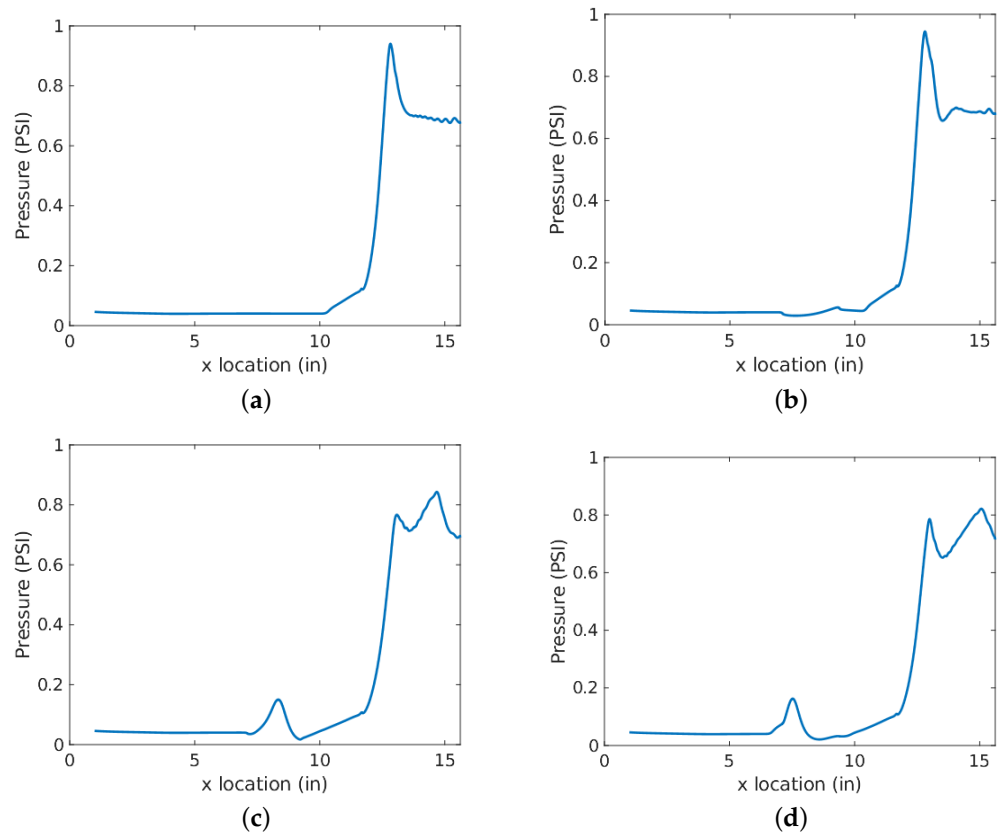

Figure 13. RANS surface pressure profiles for the maximal and minimal pressure integral cases. Flare corner located at $x = 11.68$ in. (**a**) Flat, $A_1 = 0$, $A_2 = 0$. (**b**) Maxima pressure integral case, $A_1 = -0.756$, $A_2 = 0.735$. (**c**) Minima pressure integral case 1, $A_1 = 2.914$, $A_2 = -1.262$. (**d**) Minima pressure integral case 2, $A_1 = 2.699$, $A_2 = 2.018$.

A modest disagreement in the Kriging-modeled heat flux peak compared to the RANS heat flux peak was observed in the minima cases, listed in Table 8. There was an approximately 8% difference between the Kriging and RANS predictions at these minima values. This is likely attributable to the fact that these minima values are situated on the domain corners, rather than within them, where Kriging performance is expected to degrade. The streamlines from the RANS simulations are compared in Figure 12. Note

that the undeformed case, shown in Figure 12a, closely aligned with the maximal heat flux peak case, and slight distortion and streamline alteration achieved a peak, as shown in Figure 12b. In contrast, the peak temperature contours off-body are substantially widened in Figure 12c,d, and the peak heat fluxes are reduced, while secondary peaks in heat flux begin to appear downstream.
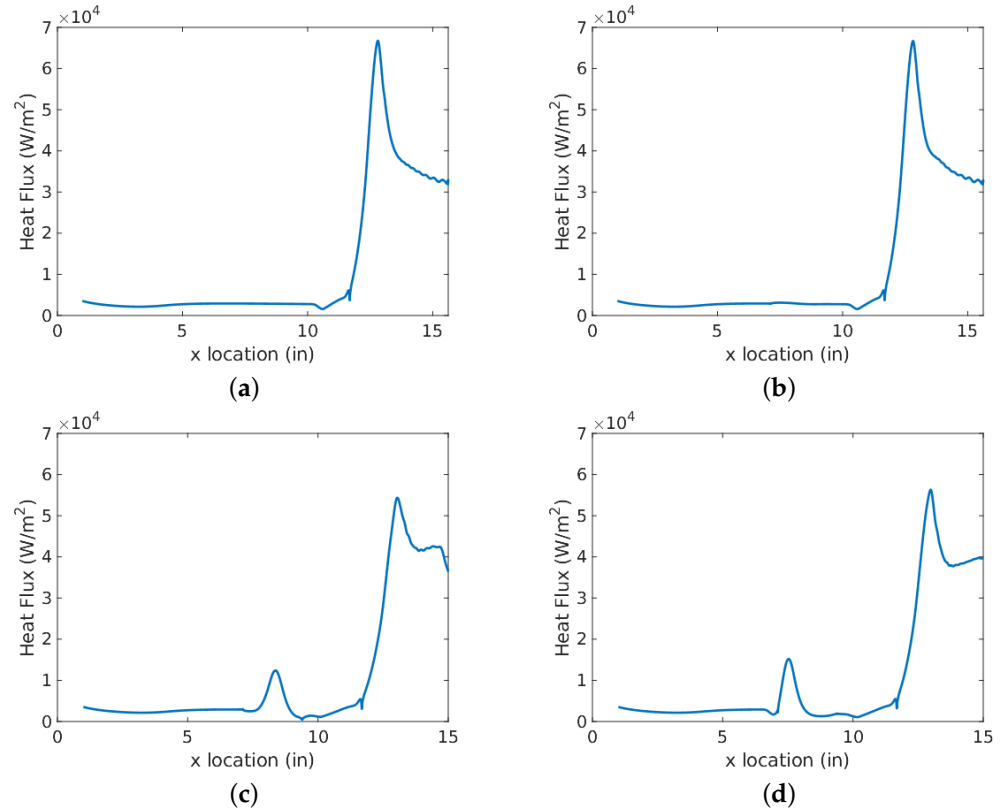

(a)

(b)

(c)

(d)

Figure 14. RANS surface heat flux profiles for the maximal and minimal heat flux integral cases. Flare corner located at $x = 11.68in$. (**a**) Flat, $A_1 = 0$, $A_2 = 0$. (**b**) Maxima heat flux integral case, $A_1 = 0.164$, $A_2 = 0.107$. (**c**) Minima heat flux integral case 1, $A_1 = 3.131$, $A_2 = -2.118$. (**d**) Minima heat flux integral case 2, $A_1 = 3.131$, $A_2 = 2.018$.

Table 8. Maxima and minima heat flux peak predictions.

	Kriging Prediction		RANS Prediction	
Configuration	**Peak Heat Flux (W/m^2)**	**% Difference from Flat**	**Peak Heat Flux (W/m^2)**	**% Difference from Flat**
Flat, $A_1 = 0$, $A_2 = 0$	6.67×10^4	N/A	6.68×10^4	N/A
Max heat flux peak case, $A_1 = -0.540$, $A_2 = 0.307$	6.67×10^4	+0.56%	6.71×10^4	+0.56%
Min heat flux peak case 1, $A_1 = 3.131$, $A_2 = -2.118$	5.89×10^4	-11.8%	5.44×10^4	18.6%
Min heat flux peak case 2, $A_1 = 3.131$, $A_2 = 2.018$	5.96×10^4	-10.7%	5.63×10^4	15.7%

The response surface for integrated heat flux is shown in Figure 9. The upper and lower bounds varied by approximately 2% of the maximum value, similar to the integrated pressures. The global maximal integral heat flux was near the undeformed state, with the maxima at only a 0.01% increase in the heat flux integral compared to the undeformed case. This again indicates that perturbations to the boundary layer in this upstream region mostly cause reductions in the integral heat flux, albeit to a lesser extent than the peak values.

Heat flux integral comparisons between the Kriging and RANS predictions, in Table 9, indicate that, while the accuracy of the modeled heat flux peak values was sensitive to being on the corners of the domain, the integral values differed by only about 1%. Heat flux profiles of RANS simulations at the Kriging model predicting integral maxima and minima are shown in Figure 14. The heat flux profile for the maxima integral, Figure 14b, exhibited marginal changes in the heat flux profile compared to the undeformed example. The minima examples, Figure 14c,d, have reduced peak values of heat flux; however, the heat flux peak was seemingly redistributed further downstream. This ultimately resulted in only a minor influence on the total reduction in the heat flux integral.

Table 9. Maxima and minima heat flux integral predictions.

	Kriging Prediction		**RANS Prediction**	
Configuration	**Integrated Heat Flux over Flare (W/m^2-in)**	**% Difference from Flat**	**Integrated Heat Flux over Flare (W/m^2-in)**	**% Difference from Flat**
Flat, $A_1 = 0$, $A_2 = 0$	1.457×10^5	N/A	1.457×10^5	N/A
Max heat flux integral case, $A_1 = 0.164$, $A_2 = 0.107$	1.460×10^5	+0.01%	1.458×10^5	+0.01%
Min heat flux integral case 1, $A_1 = 3.131$, $A_2 = -2.118$	1.427×10^5	-2.1%	1.409×10^5	-3.3%
Min heat flux integral case 2, $A_1 = 3.131$, $A_2 = 2.018$	1.428×10^5	-2.0%	1.409×10^5	-3.3%

Finally, predicted separation lengths from the Kriging model for each input value are shown in Figure 10. The boundary layer flow over deformed surfaces is affected due to pressure gradients from a variety of sources, either due to the compression or expansion waves from the flow turning at the initiation of the distortion or due to the subsequent surface curvature itself. The boundary layer undergoes a deceleration as it passes through compression shocks and over positive surface curvature, and it accelerates through expansions and over negative surface curvature. For a pinned panel configuration, the edges of the distortion show discontinuous changes in slope—leading to either compression or expansion waves at the edges of the distortion, with smoothly varying curvature within. The combination of discontinuous slope changes and smoothly varying curvatures causes changes in the shape and velocities of the boundary layer downstream, as is evident in the changes to the streamlines and the separation corner downstream of the distortions. The results in Figure 10 suggest that mode 1 amplitude (A_1) strongly influences the separation length, with a minor influence from the mode 2 amplitude (A_2). As the mode 1 amplitude decreases (indicating a more negative distortion), the separation length diminishes, while an increase in the mode 1 amplitude (signifying a more positive distortion) extends the separation length. In contrast, the mode 2 amplitude has a pronounced impact on the separation length when the mode 1 amplitude is negative but less so when the mode 1 amplitude is positive, with almost no impact for the largest mode 1 amplitudes.

A comparison of the predictions for the separation lengths from the Kriging model and RANS simulations is shown in Table 10. Here, a roughly 3% variation was observed in the maximal separation length cases between RANS and Kriging. The streamlines from the RANS simulations were analyzed, as shown in Figure 15. For the minimal-separation-length case, Figure 15b, the streamlines converged significantly, indicating a shrinking of the boundary layer, and they led to a boundary layer that was more resilient to separation due to pressure gradients. In Figure 15c,d, the streamlines immediately after the distortion are spread out compared to the undeformed case, and the separation bubble is enlarged. This streamline pattern indicates a thicker boundary layer with a higher shape factor, which is more likely to separate at the corner of the flare due to the shock-induced pressure gradient.

Table 10. Maxima and minima separation length predictions.

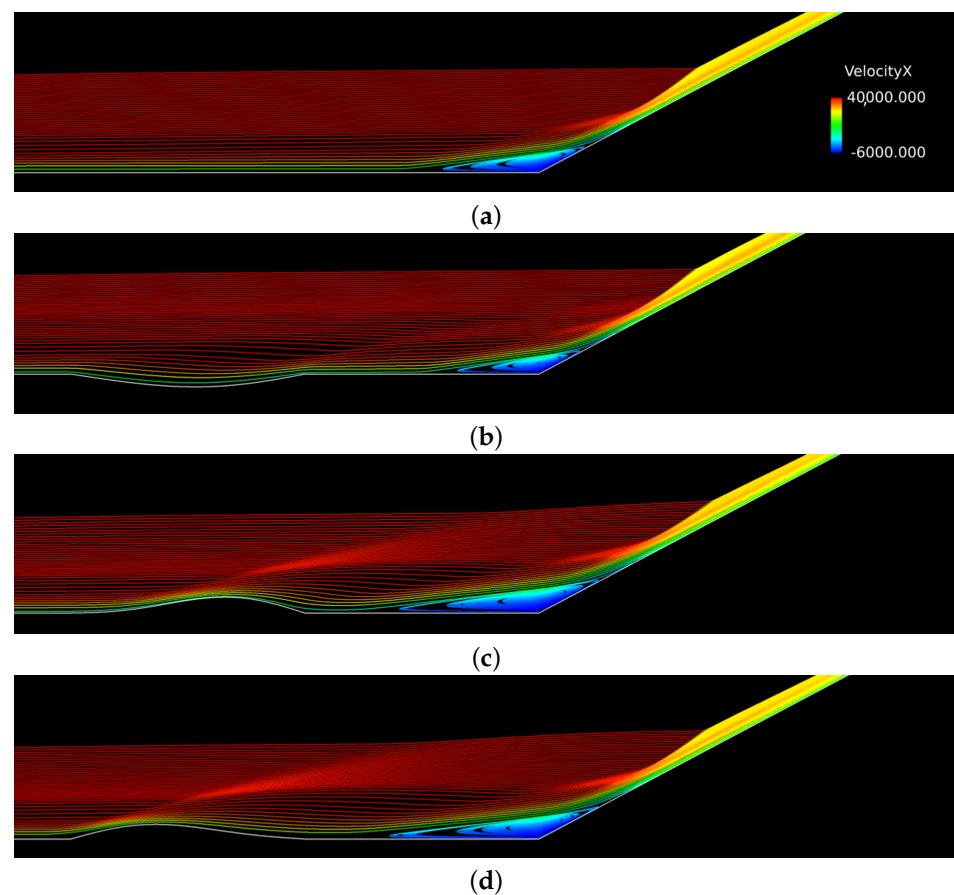|	Kriging Prediction		RANS Prediction	
Configuration	Separation Length (in)	% Difference from Flat	Separation Length (in)	% Difference from Flat
Flat, $A_1 = 0$, $A_2 = 0$	1.93	N/A	1.93	N/A
Min separation peak case, $A_1 = -3.131$, $A_2 = 0.164$	1.70	-11.9%	1.70	-11.9%
Max separation peak case 1, $A_1 = 3.131$, $A_2 = -1.405$	2.47	$+27.7\%$	2.56	$+32.6\%$
Max separation peak case 2, $A_1 = 3.131$, $A_2 = 1.0$	2.41	$+24.6\%$	2.47	$+27.7\%$

(**a**)

(**b**)

(**c**)

(**d**)

Figure 15. Streamlines of the maximal and minimal separation length cases. Note that the corner separation is shown with the blue recirculation bubble. (**a**) Flat, $A_1 = 0$, $A_2 = 0$. (**b**) Minima separation length case, $A_1 = -3.131$, $A_2 = 0.164$. (**c**) Maxima separation length case 1, $A_1 = 3.131$, $A_2 = -1.405$. (**d**) Maxima separation length case 2, $A_1 = 3.131$, $A_2 = 1.0$.

One of the main drivers of the alterations in the separation onset appears to be the type of topology of the distortions. Consider, in the top half of Figures 10 and 15b, that for distortions with strong recessions, the separation length is reduced, which is accompanied by a convergence of streamlines and a shrinking of the boundary layer. This is contrasted with the bottom half of Figures 10 and 15c,d, which show that, for distortions with strong protrusions, the separation length is increased and is accompanied by a widening of streamlines, indicating a larger boundary layer. For intermediate distortions that have both protrusion and recession, the streamlines have a shifting convergence and expansion, indicating a more complicated effect on the boundary layer.

Next, consider the aggregated results listed in Table 11, providing insights into how targeting specific maxima or minima impacts the outcomes of other parameters. The cells in Table 11 are color-coded, based on their percentage differences from the undeformed values. The color gradient transitions from red (indicating a positive % difference) to white (indicating a 0% difference) to green (indicating a negative % difference), scaled according to the maximum and minimum values of the table. There was a consistent increase in the separation lengths for all the minimal peak and integral cases. Specifically, achieving an 18% reduction in the peak heat corresponded to a 43% increase in the separation length at the corner. Additionally, the Kriging-model-predicted maximas and minimas were corroborated with the a posteriori RANS predictions at these sites, as the pressure and heat flux peak and integral maxima and minima values were consistently the maxima and minima of the RANS cases simulated. However, there was an anomaly in the separation length predictions, and the Kriging-predicted maximum separation length did not correspond to the RANS-simulated maximum separation length, which occurred for a distortion of $A_1 = 3.131$ and $A_2 = -1.405$. This discrepancy can be traced back to the inherent limitation and reduction in the accuracy of surrogate models at domain boundaries and corners.

Table 11. RANS predicted values for each maximal/minimal condition identified from the Kriging response surfaces. The cells are color-coded, based on their percentage differences from the undeformed values. The color gradient transitions from red (indicating a positive % difference) to white (indicating a 0% difference) to green (indicating a negative % difference), scaled according to the maximum and minimum values of the table.

RANS Simulation Case	Pressure Peak % Change	Pressure Integral % Change	Heat Flux Peak % Change	Heat Flux Integral % Change	Separation Length % Change
Max pressure peak, $A_1 = -0.756, A_2 = 0.735$	0.91	0.14	0.30	−0.18	−4.9
Min pressure peak, $A_1 = 2.699, A_2 = 2.018$	−13.3	−2.9	−13.8	−2.7	26.2
Max pressure integral, $A_1 = -1.620, A_2 = 0.0$	0.45	0.19	−0.21	−0.17	−7.3
Min pressure integral, $A_1 = 3.131, A_2 = 2.018$	−12.6	−3.5	−15.7	−3.4	30.3
Max heat flux peak, $A_1 = -0.540, A_2 = 0.307$	0.87	0.14	0.56	−0.01	−3.4
Min heat flux peak, $A_1 = 3.131, A_2 = -2.118$	−10.3	−3.5	−18.6	−3.3	43
Max heat flux integral, $A_1 = 0.164, A_2 = 0.107$	−0.06	−0.03	−0.08	0.01	1.0
Min heat flux integral, $A_1 = 3.131, A_2 = 2.018$	−12.6	−3.5	−15.7	−3.4	30.3
Min separation length, $A_1 = -3.131, A_2 = 0.164$	−0.47	0.07	−1.9	−1.0	−11.9
Max separation length, $A_1 = 3.131, A_2 = -1.405$	−12.5	−2.4	−13.6	−2.0	32.6

3.2. Impact of Distortion Location

The study's analysis was extended to also consider the distance of upstream distortion from the flare corner, ℓ. Parametric bounds for this case are listed in Table 2. The Kriging models were generated from 300 additional RANS simulations. The generation and parameters of these new models are discussed in Appendix B.2. The selected model is defined in Equation (4):

$$0.0016 + 2.958 \cdot Matern(lengthscale = 1.44, \nu = 1.5) + WhiteKernel(noiselevel = 0.0187) \tag{4}$$

For brevity, only the pressure peak and the corner separation length results are reported here. However, the trends for the heat flux peak, integrated heat flux, and integrated

pressure were consistent with the trends observed herein for the pressure peak examples. Three-dimensional response surfaces were generated for this model, and in order to visualize them in two dimensions, one variable could be held constant while varying the other variables.

The predicted peak pressure values from the Kriging model, as a function of both the input distortion amplitudes and the location of the distortion, are shown in Figure 16. The x-axis corresponds to the length of the distortion from the flare, ℓ, and the y-axis is either the mode 1 or mode 2 amplitudes (A_1 or A_2). In Figure 16a, A_2 is held constant at 0, and in Figure 16b, A_1 is held constant at 0. From left to right on the contours, there are demarcations at approximately $\ell = 0.5$ and $\ell = 1.5$. In the first zone, near the flare corner where $0 \leq \ell < 0.5$, Figure 16a,b shows inverse patterns of each other. Negative mode 1 distortions were correlated with decreased peak pressures on the flare, as seen in the top left corner of Figure 16a, whereas positive mode 1 distortions resulted in increased peak pressures, seen in the bottom left corner of Figure 16a. In contrast, negative mode 2 distortions led to an increase in the pressure peak, seen in the top left corner of Figure 16b, whereas positive mode 2 distortions resulted in a decrease, seen in the bottom right corner of Figure 16b. This pattern suggests that positive, convex distortions near the flare corner (positive mode 1 and negative mode 2) increased the pressure peak, and negative, concave distortions near the flare corner (negative mode 1 and positive mode 2) decreased the pressure peak on the flare. As the distance from the flare corner of the distortion increases past $\ell > 0.5$, the responses were inverted, and the response surfaces reverted to the trends seen previously in Section 3.1 for $\ell = 1$. Finally, as the distortions were moved even further from the flare corner, beyond $\ell > 1.5$, the influence of upstream distortion on the flare peak pressure diminished. Note that the convex, positive mode 1 distortion ($A_1 > 0$) had the most lasting impact on the flare pressure peak values.
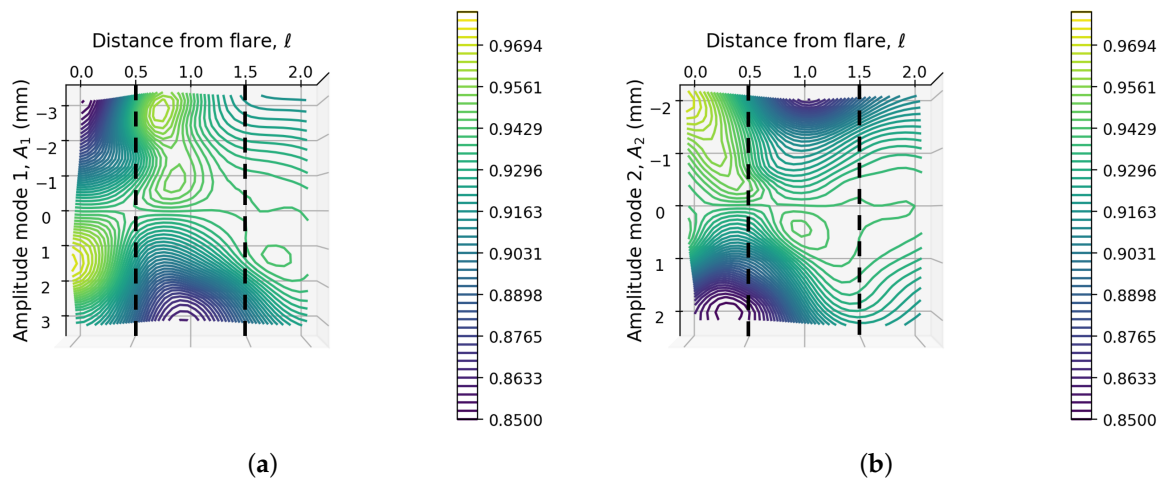

Figure 16. Kriging model pressure peaks (psi). Dotted lines indicate demarcations of distinct responses. (**a**) Distortion location, ℓ (panel lengths) vs. mode 1 amplitude, A_1 (mm). (**b**) Distortion location, ℓ (panel lengths) vs. mode 2 amplitude, A_2 (mm).

Deeper insights were gained using RANS simulations of flat ($A_1 = 0$, $A_2 = 0$), convex, positive mode 1 ($A_1 = 2$, $A_2 = 0$), concave, negative mode 1 ($A_1 = -2$, $A_2 = 0$), combined convex–concave, positive mode 2 ($A_1 = 0$, $A_2 = 2$), and combined concave–convex, negative mode 2 ($A_1 = 0$, $A_2 = -2$) distortions. Here $\ell = 0$ and $\ell = 2$. The resulting shock structures for distortions against the flare corner ($\ell = 0$) are depicted in Figure 17 and far from the corner ($\ell = 2$) in Figure 18. The introduction of the distortion within the corner separation region, Figure 17, was the root cause of the delineation seen at $\ell \approx 0.5$ on the pressure peak response surface in Figure 16. In Figure 17b,e, the convex distortions are located within the recirculation, and they reduce the separation length. The distortions near the flare were accompanied by compression shock wave formations that impinged at the pre-existing pressure peak location. Conversely, when concave distortions were adjacent to

the flare, and within the separated region, there was an expansion in the recirculation area, as seen in Figure 17c,d. In Figure 17c, the separation trails along most of the recession, with the initiation of the separated region near the beginning of the distortion. However, the flow turn angle due to the separation is milder, indicating a weaker shock that impinges on the flare and, consequently, a smaller peak pressure. Similarly, in Figure 17d, the separation region overlaps with the second half of the distortion. However, the turn angle dedicated to the separation is weaker than that of the turn angle at the start of the distortion. As such, the shock waves are spread out on the flare, leading to a smaller pressure rise than that caused by only the separation corner.
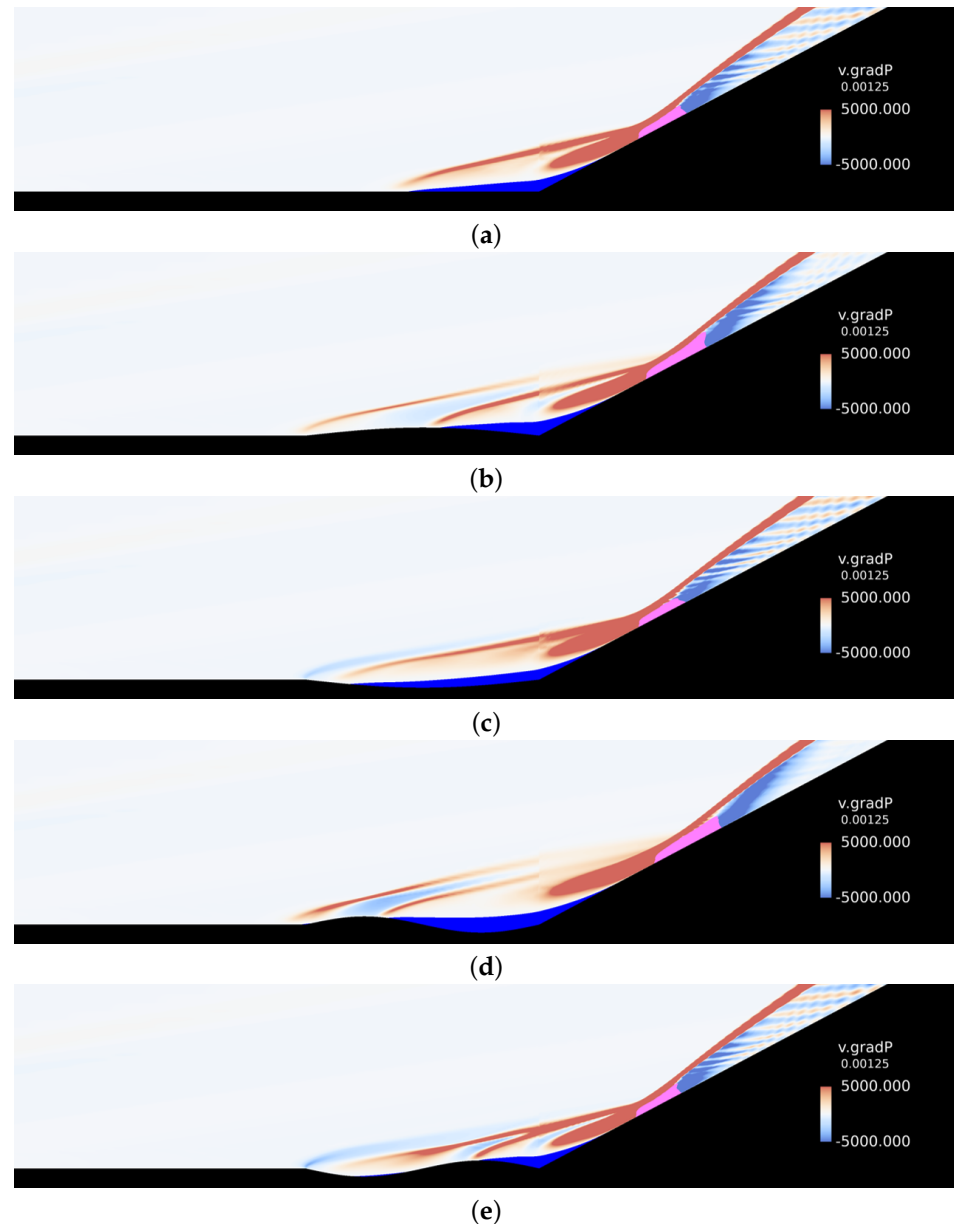

Figure 17. Shock structures of distortions against the flare corner ($\ell = 0$), shown as the velocity dot product with the gradient of pressure, with expansions shown in blue (negative) and compressions shown in red (positive). Corner separation ($u < 0$) is overlaid in dark blue, and peak pressures (greater than 0.8 psi) are overlaid in pink. (**a**) Flat, $A_1 = 0$, $A_2 = 0$. (**b**) Convex, positive mode 1 distortion, $A_1 = 2$, $A_2 = 0$, $\ell = 0$. (**c**) Concave, negative mode 1 distortion, $A_1 = -2$, $A_2 = 0$, $\ell = 0$. (**d**) Convex–concave, positive mode 2 distortion, $A_1 = 0$, $A_2 = 2$, $\ell = 0$. (**e**) Concave–convex, negative mode 2 distortion, $A_1 = 0$, $A_2 = -2$, $\ell = 0$.

In Figure 18, the shock structures of the distortions located two panel lengths from the flare ($\ell = 2$) are shown. As expected from Figure 16, upstream distortions at two panel lengths from the flare ($\ell = 2$) negligibly affected the downstream peak pressures, as the corner separation shock wave was much stronger relative to the distortion-generated shock. Further, these secondary shocks dissipated before reaching the flare. The compression and expansion waves from the distortions caused pressure variations on the flare surface. However, the impact was notably less pronounced compared to distortions closer to the flare or distortions that generated shock impingements at the same location as the corner separation shock. The dissipation and weakened responses caused by distortion-induced shock waves were the underlying causes of the reduced responses for distortions far from the flare ($\ell > 1.5$).
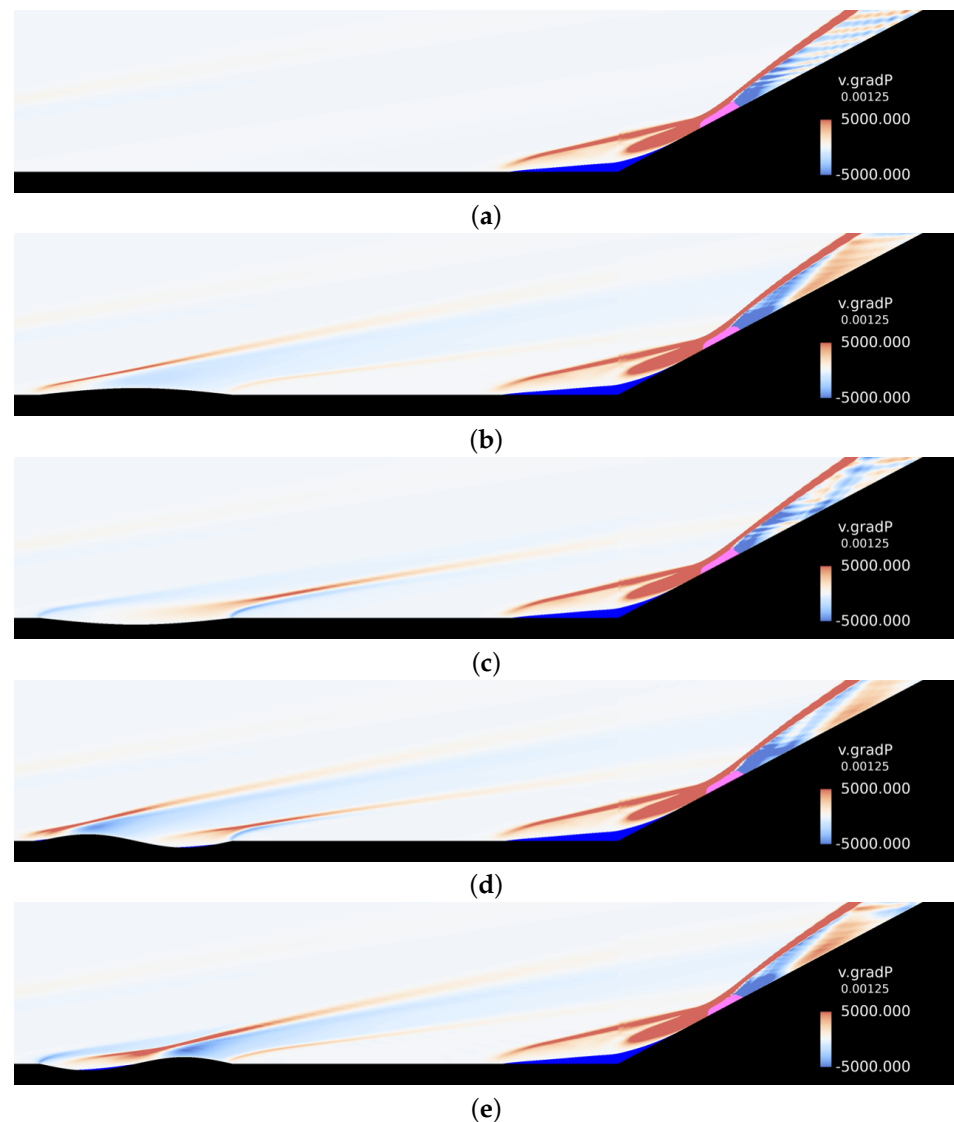

Figure 18. Shock structures of distortions two panel lengths ($\ell = 2$) from the flare corner, shown as the velocity dot product with the gradient of pressure, with expansions shown in blue (negative) and compressions shown in red (positive). Corner separation ($u < 0$) is overlaid in dark blue, and peak pressures (greater than 0.8 psi) are overlaid in pink. (**a**) Flat, $A_1 = 0$, $A_2 = 0$. (**b**) convex, positive mode 1 distortion, $A_1 = 2$, $A_2 = 0$, $\ell = 2$. (**c**) Concave, negative mode 1 distortion, $A_1 = -2$, $A_2 = 0$, $\ell = 2$. (**d**) Convex–concave, positive mode 2 distortion, $A_1 = 0$, $A_2 = 2$, $\ell = 2$. (**e**) Concave–convex, negative mode 2 distortion, $A_1 = 0$, $A_2 = -2$, $\ell = 2$.

The predicted corner separation length using the Kriging model is shown in Figure 19, where the mode 2 amplitude, A_2, is held constant at 0 in Figure 19a, and the mode 1 amplitude, A_1, is held constant at 0 in Figure 19b. Three different responses appeared when varying ℓ and A_1, as shown in Figure 19a: the first ranging from $0 \leq \ell < 0.3$ for distortions against the flare; a second extending from $0.3 < \ell < 1.5$; and a third for distortions far from the flare for $\ell > 1.5$. However, only two responses occurred when varying ℓ and A_2, as shown in Figure 19b: the first for distortions near the flare, $0 \leq \ell < 0.6$, and the other for distortions away from the flare, $\ell > 0.6$. For both, a pattern emerged when the distortion was adjacent to the flare and situated within the corner separation. As convex distortions approached the corner, the separation length was reduced, and as concave distortions approached the corner, the separation length increased. The underlying cause of this effect is apparent from analyzing the responses of the streamlines for the distortions near the corner, shown in Figure 20. The streamlines demonstrate that convex distortions near the flare significantly reduced the overall separation length, as shown in Figure 20b,e. In contrast, concave distortions extended the separation further upstream, as shown in Figure 20c,d. These behaviors were expected, as concave/convex surfaces introduce pressure gradients on the boundary layer, affecting skin friction and separation [7,27,68], which are the basic principles of shock control bumps [69–72]. As the distortions shifted beyond approximately $\ell > 0.6$, the trends in the separation length shifted towards the results discussed in Section 3.1 and shown in Figure 6 for $\ell = 1$. Finally, for distortions beyond $\ell > 1.5$ in Figure 19a, a rapid return to the undeformed cylinder/flare separation length occurred. The restoration of the response to the undeformed separation length occurred faster for concave distortions compared to convex distortions where the separation length was restored at a slower rate. Note, in Figure 21, that the streamlines reverted to the nominal state approximately halfway between the distortion and the separation region, confirming the diminished influence of the distortion on the downstream flow as the distance from the separation and flare corner increased beyond $\ell = 0.6$, as predicted in Figure 19b. The concave, negative mode 1 distortion response returned to undisturbed streamlines quickly following the distortion, as shown in Figure 21c. However, the convex, positive mode 1 distortion had a more lasting effect on the streamlines, as shown in Figure 21b. Furthermore, for the mode 2 distortions, Figure 21d,e, the streamlines returned to their nominal state quicker compared to the mode 1 distortions. This is reflected in Figure 19b, as the separation length contour beyond $\ell = 0.6$ shows little change compared to the undeformed case for any distortion at any location.
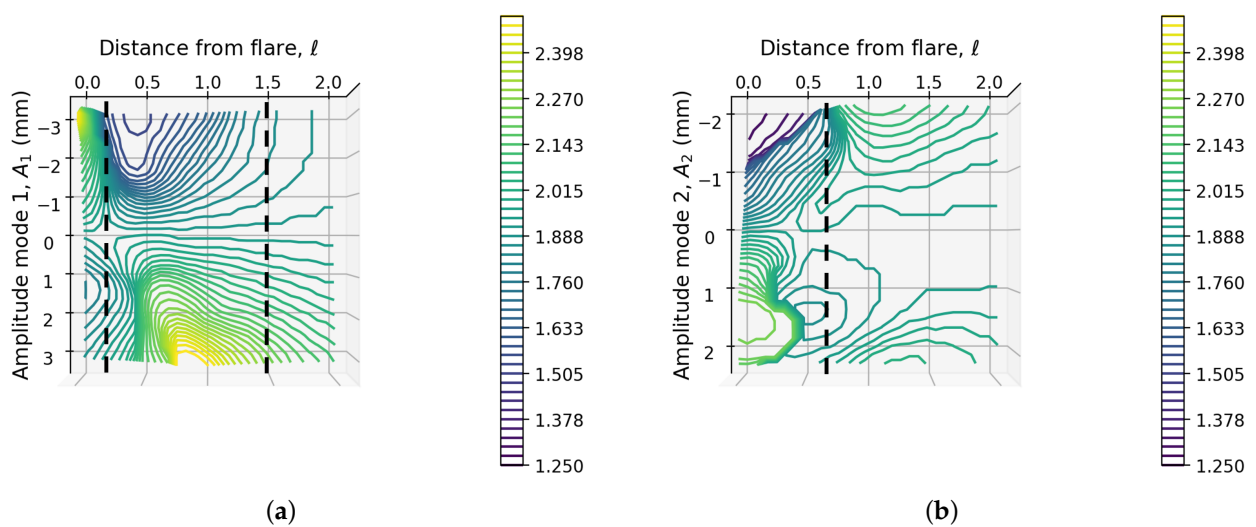

(a)   (b)

Figure 19. Kriging model separation lengths (in). Dotted lines demarcate distinct responses. (**a**) Distortion location, ℓ (panel lengths) vs. mode 1 amplitude, A_1 (mm). (**b**) Distortion location, ℓ (panel lengths) vs. mode 2 amplitude, A_2 (mm).
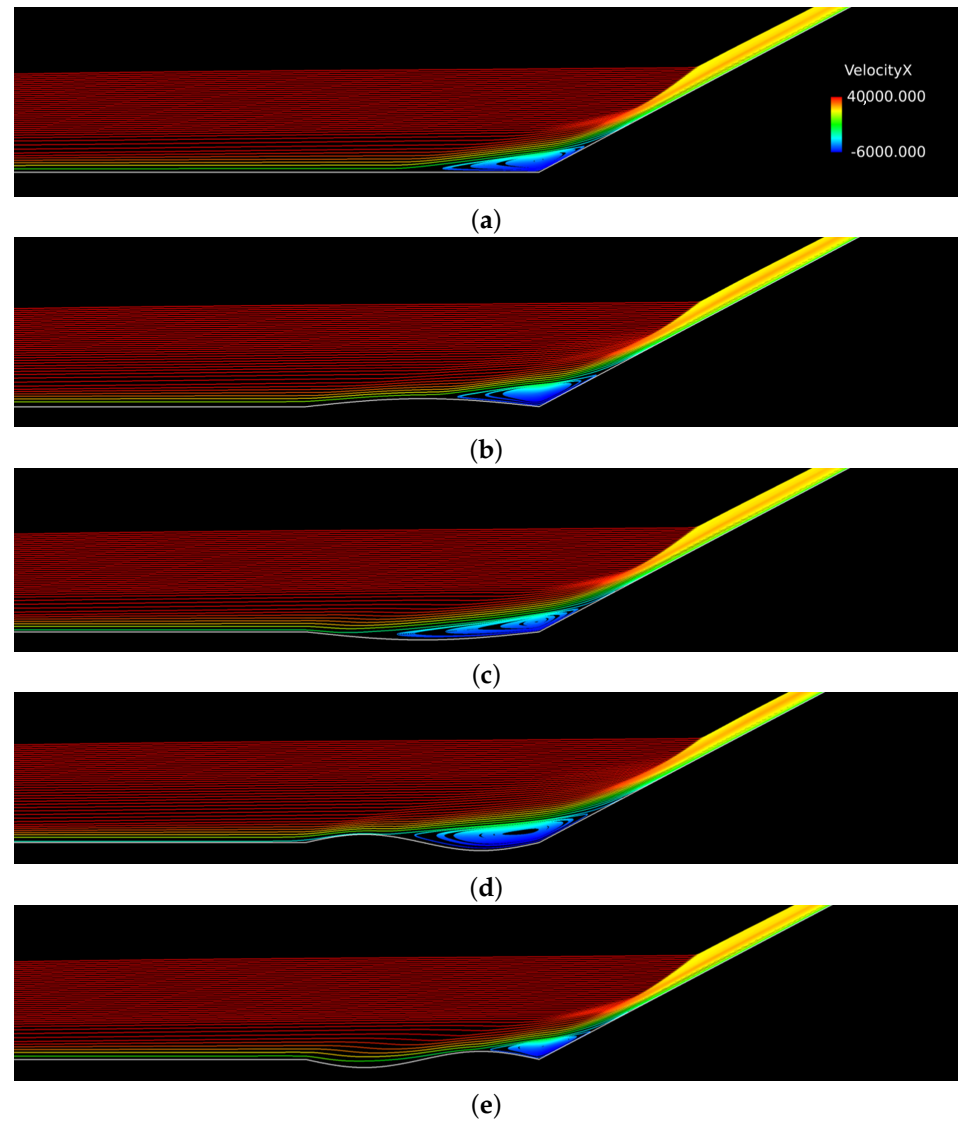
Figure 20. Streamlines of distortions against the flare corner ($\ell = 0$). Note that the corner separation is shown in the blue recirculation bubble. (**a**) Flat, $A_1 = 0$, $A_2 = 0$. (**b**) Convex, positive mode 1 distortion, $A_1 = 2$, $A_2 = 0$, $\ell = 0$. (**c**) Concave, negative mode 1 distortion, $A_1 = -2$, $A_2 = 0$, $\ell = 0$. (**d**) Convex–concave, positive mode 2 distortion, $A_1 = 0$, $A_2 = 2$, $\ell = 0$. (**e**) Concave–convex, negative mode 2 distortion, $A_1 = 0$, $A_2 = -2$, $\ell = 0$.
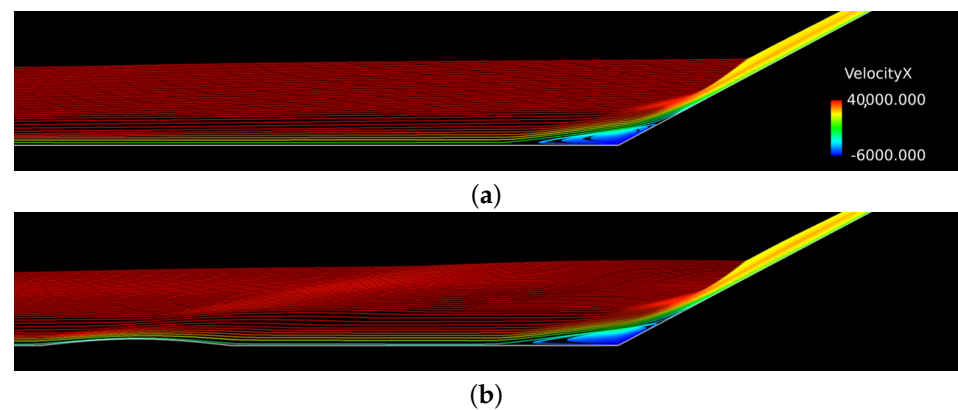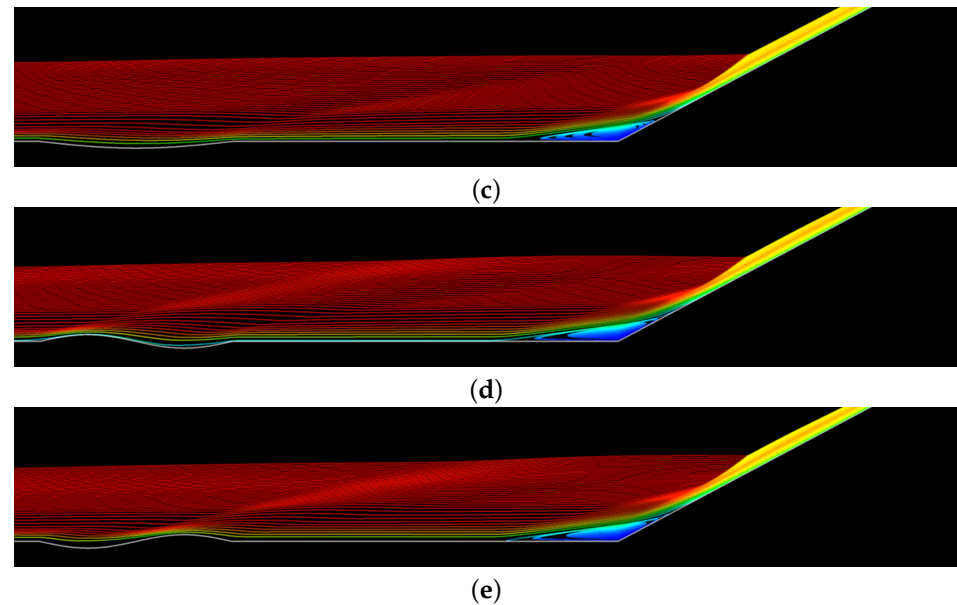

Figure 21. *Cont*.

Figure 21. Streamlines of distortions two panel lengths from the flare corner ($\ell = 2$). Note that the corner separation is shown in the blue recirculation bubble. (**a**) Flat, $A_1 = 0$, $A_2 = 0$. (**b**) Convex, positive mode 1 distortion, $A_1 = 2$, $A_2 = 0$, $\ell = 2$. (**c**) Concave, negative mode 1 distortion, $A_1 = -2$, $A_2 = 0$, $\ell = 2$. (**d**) Convex–concave, positive mode 2 distortion, $A_1 = 0$, $A_2 = 2$, $\ell = 2$. (**e**) Concave–convex, negative mode 2 distortion, $A_1 = 0$, $A_2 = -2$, $\ell = 2$.

4. Concluding Remarks

An approach to parametrically characterizing the impact of static surface distortions on a downstream cylinder/flare configuration was developed. The distortions are representative of structural deformations induced via fluid–structural and fluid–thermal–structural interactions. A trend analysis was carried out using RANS simulations in conjunction with Kriging response surfaces. Analyses of Kriging-model-generated response surfaces were conducted by varying the modal amplitudes of the distortion and the location of the distortion with respect to the cylinder/flare. Attention was focused on the peak and integral values of the pressure and heat flux, as well as changes in the cylinder/flare corner separation length. The Kriging model was used to identify key trends and parametric combinations of interest. The phenomena contributing to the trends and predictions were affirmed through a posteriori RANS simulations of parametric combinations, selected from maximal/minimal conditions in the different model response surfaces.

These analyses yielded the following conclusions:

1. The introduction of upstream surface distortion tended to decrease peak pressure and heat flux values, in extreme cases by $O(10\%)$. However, integrated pressure and heat flux were only marginally impacted (1%). This behavior was attributed to reductions in primary peaks and the introduction of secondary peaks.

2. The flare corner separation length was highly sensitive to upstream distortions, decreasing by up to 12% and increasing by upwards of 43% compared to the undeformed cylinder/flare.

3. RANS characterizations highlighted several marked impacts of upstream distortion on the downstream flow response. The local compression and expansion surfaces give rise to shocks and expansion waves, which impinge on and affect the loading on the flare surface by augmenting the primary peaks at the separation shock impingement, as well as introducing additional peaks further downstream. Upstream deformation-induced perturbations to the boundary layer that influence the downstream separation corner and reattachment behavior affect the separation length and heat flux profiles.

4. Single protrusions into the flow predominantly lead to longer separation lengths at the corner, while a single recession tends to reduce it. Upstream distortions cause varying

degrees of alteration to the boundary-layer state, evident in the convergence and expansion of the streamlines of the flow and demonstrating the ability of the distortion to affect the boundary-layer state as it travels to the flare corner and influences separation behavior.

5. The output functions of interest show some correlation behavior, as decreases in the peak and integrated values of pressure and heat flux correspond with large increases in separation lengths. Conversely, decreases in separation lengths correspond to only small changes in the peak and integrated values of pressure and heat flux.

6. Distortions within the separation region ($\ell < 0.5$) cause distinct flow responses compared to distortions outside of the separated region. Convex distortions reduce the separation size, while concave distortions extend the separation upstream.

7. The impact of distortion diminishes rapidly when placed approximately 1.5 panel lengths ($\ell > 1.5$) or farther from the flare. Distortions protruding into the flow tend to cause more lasting effects, while recessed distortions cause the flow to return to a nominal state sooner. Mode 2 distortions with combined protruded and recessed distortions cause less of an impact downstream overall compared to the mode 1 cases when far from the flare.

Overall, the results and conclusions of this study elucidate a variety of roles that upstream surface distortions play on downstream flow responses both in the projected shocks and expansions and in boundary-layer alterations.

Abbreviations

The following abbreviations are used in this manuscript:

A	peak distortion amplitude
A_1	peak distortion amplitude, mode 1 contribution
A_2	peak distortion amplitude, mode 2 contribution
c_p	specific heat capacity at constant pressure
E_{mean}	mean error
L	distortion length
ℓ	distance of distortion end from flare (panel lengths)
M	Mach number
m	mode number
N	number of grid points
p	pressure
q	heat flux
Re	Reynolds number
St	modified Stanton number
T	temperature

u	streamwise velocity
$\vec{v}$	velocity vector
x	streamwise coordinate
y	wall-normal coordinate
δ_v	surface distortion
δx	streamwise direction grid spacing
δy	wall-normal direction grid spacing
δ_{99}	boundary-layer thickness
$\triangledown$	gradient operator
ν	Matern Kernel smoothness parameter
ρ	density

Subscripts

aw	adiabatic wall condition
w	wall condition
0	total/stagnation condition
∞	freestream condition

Appendix A. Grid Refinement and Time Step Study

Appendix A.1. Grid Refinement Study

The grid resolution required for the simulations in this study was established through a grid convergence study based on three different grid sizes and distortions at two different locations with respect to the flare corner. Both simulations were conducted at a higher Mach number, Reynolds number, and freestream temperature, as well as the steepest distortions to account for a worst-case scenario. The parameters for the grid study are shown in Table A1. The y^+ values at the wall for the grids were estimated for the flare to be 1 for the coarse grid, 0.5 for the medium grid, and 0.25 for the fine grid. The simulated shear stress, density, and viscosity at the wall determined the actual y^+ values, reported in Tables A2 and A3. A y^+ value less than 1 should be implemented to resolve the viscous sublayer. However, y^+ values in boundary layers experiencing adverse pressure gradients and streamline curvature are difficult to assess for accuracy purposes. They were important in the present study, however, since Kestrel invokes wall functions for y^+ values larger than 3. These pressure gradients occurred in this configuration near the flare corner and shock impingement location, causing spikes in the y^+ value. For the coarse grid, this value was larger than 1, but less than 3, indicating that this grid does not use wall functions but insufficiently resolves the viscous sublayer. The grid metrics and errors concerning the finest grid for the distortion of $\ell = 0.1$ are shown in Table A2, while the error metrics for distortion of $\ell = 2$ are shown in Table A3. The error metrics of the pressure, heat flux, and skin friction indicate that the grid has a marginal impact on the profiles simulated here. The medium grid was, therefore, selected to balance the above considerations with a reduced simulation expense.

Table A1. Grid study flow and distortion parameters.

M_∞	Re	T_∞ (K)	ℓ (Panel Lengths)	L (mm)	A_1 (mm)	A_2 (mm)
8.0	1×10^6	83.3	0.1/2	19	3.3	2.2

Table A2. Metrics for the grid refinement study—$\ell = 0.1$.

					Pressure		Heat Flux		Skin Friction Coefficient X	
	$N_x \times N_y$	δx	δy at Wall	Actual y^+	R^2	E_{mean} (%)	R^2	E_{mean} (%)	R^2	E_{mean} (%)
Coarse	3111×200	5×10^{-3}	4×10^{-5}	1.35	0.9998	0.63	0.9992	1.51	0.9990	1.70
Medium	7776×215	2×10^{-3}	2×10^{-5}	0.67	0.9998	0.28	0.9995	0.38	0.9998	0.29
Fine	$15{,}551 \times 230$	1×10^{-3}	1×10^{-5}	0.34	—	—	—	—	—	—

Table A3. Metrics for the grid refinement study—$\ell = 2$.

					Pressure		Heat Flux		Skin Friction Coefficient X	
	$N_x \times N_y$	δx	δy at Wall	Actual y^+	R^2	E_{mean} (%)	R^2	E_{mean} (%)	R^2	E_{mean} (%)
Coarse	3111×200	5×10^{-3}	4×10^{-5}	1.25	0.9997	0.93	0.9991	1.47	0.9996	1.23
Medium	7776×215	2×10^{-3}	2×10^{-5}	0.62	0.9996	0.46	0.9989	0.58	0.9981	0.88
Fine	$15{,}551 \times 230$	1×10^{-3}	1×10^{-5}	0.31	—	—	—	—	—	—

Appendix A.2. Time/Iterative Convergence

Iterative simulation convergence was determined from the residuals and the integrated forces on the surfaces for the three grids and two configurations. Simulation residuals converged to values less than 10^{-4} by 2000 iterations, and integrated force values converged at around 3000 iterations, indicating that allocating 10,000 iterations ensured convergence consistently and offered a conservative estimate for these simulations.

Appendix B. Kriging Model Selection and Convergence

Appendix B.1. Surrogate Modeling Generation for Section 3.1

The Kriging surrogate model selection and convergence for Section 3.1 is discussed herein, and the inputs to the model are defined in Table 5. The top three kernel combinations, as determined according to the best Normalized Root Mean Square Error (NRMSE) and R^2 coefficient of determination values, are given in Equations (A1)–(A3). For brevity, only the Matern model with $\nu = 1.5$ will be shown in full here, Equation (A2). The SciKit-Learn package was used to automatically tune hyperparameters to the training dataset [66]. The modeled values for the test dataset compared to the RANS truth values are shown in Figure A1. A straight line of slope = 1 indicates a perfect model of the data. All three kernels work well for these datasets, with the worst $R^2 > 0.9998$, and the worst NRMSE values at 0.5% or less. Visually, note that the model behaves well over the entire range of data, with only slight deviations near 0.5 and 0.8.

$$0.272 + 2.496 \cdot RBF(lengthscale = 1.44) + WhiteKernel(noiselevel = 0.116) \tag{A1}$$

$$0.000342 + 6.656 \cdot Matern(lengthscale = 4.2, \nu = 1.5) + WhiteKernel(noiselevel = 0.103) \tag{A2}$$

$$0.0751 + 4.326 \cdot Matern(lengthscale = 2.55, \nu = 2.5) + WhiteKernel(noiselevel = 0.109) \tag{A3}$$
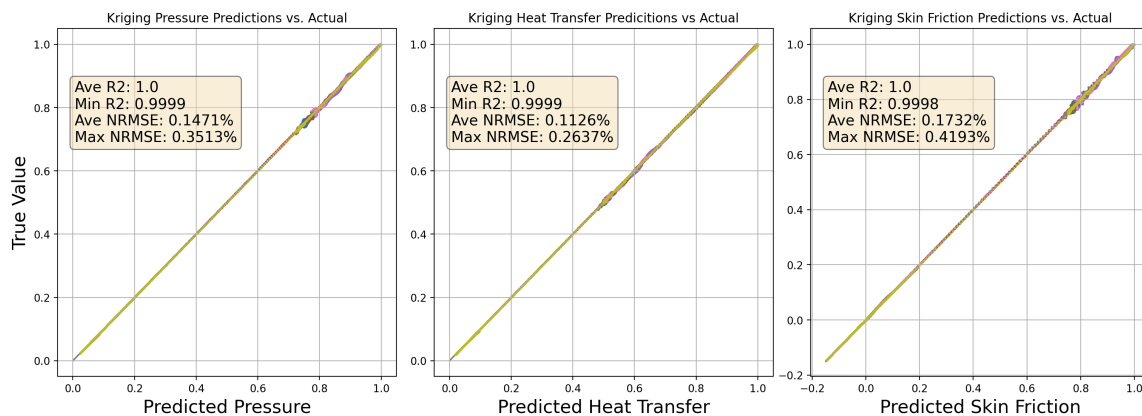

Figure A1. Initial Kriging model metrics for Matern ($\nu = 1.5$) kernel. Each line is a different test data point.

A convergence study for each was carried out individually. A sample convergence plot is shown in Figure A2. In general, for the three selected models, the worst NRMSE and worst R^2 cases converged by about a 25% data split, whereas the average NRMSE

and average R^2 converged by about a 15% data split. This implies that adding additional data points to the model beyond this 25% threshold will not enhance accuracy. In practical terms, this suggests that about 50 RANS simulations are sufficient to achieve convergence for these models.
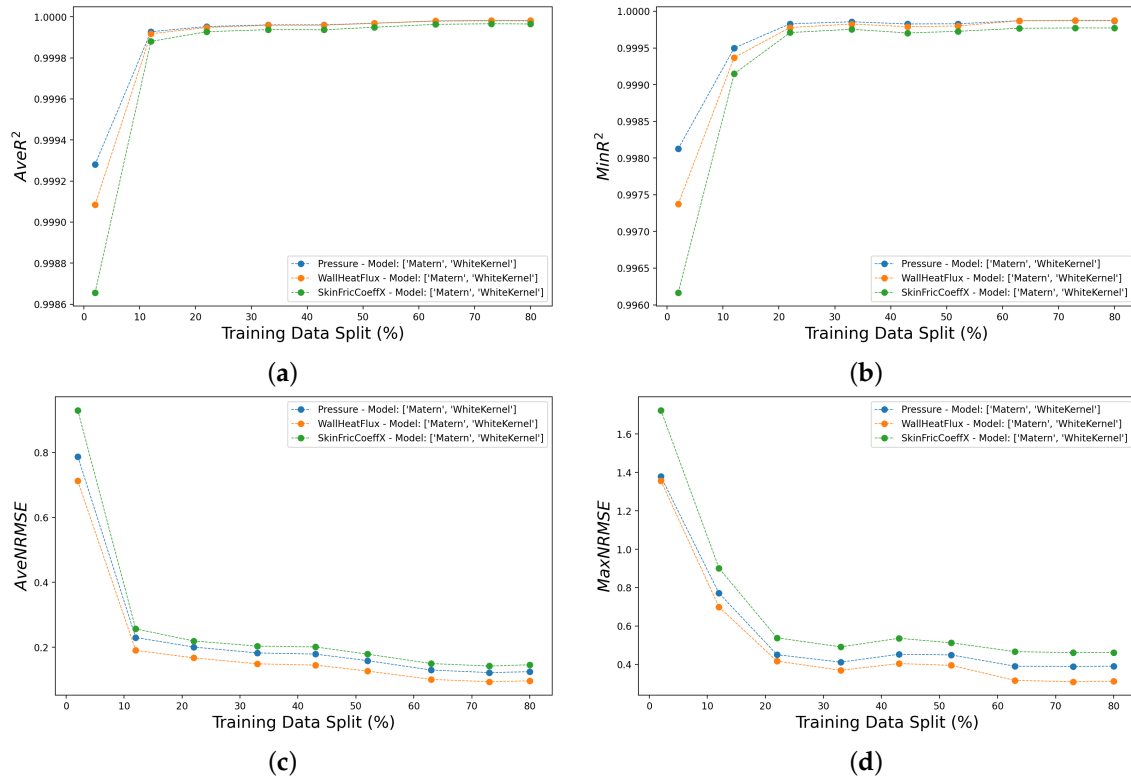

Figure A2. Model convergence study for best kernel (Matern ($\nu = 1.5$) kernel). (**a**) Average R^2. (**b**) Worst R^2. (**c**) Average NRMSE. (**d**) Worst NRMSE.

A final validation of the models was conducted using the validation data split. Pressure, heat flux, and skin friction coefficient predictions vs. the RANS values are provided for the validation data in Figure A3. This validation phase is crucial to ensuring that the model generation process is not inadvertently influenced by hyperparameter tuning, given that the validation dataset was exclusively set aside for this final assessment. The model corresponding to Equation (A2) yielded the best model metrics among the three top-performing kernels, and it was selected for the results in Section 3.1.
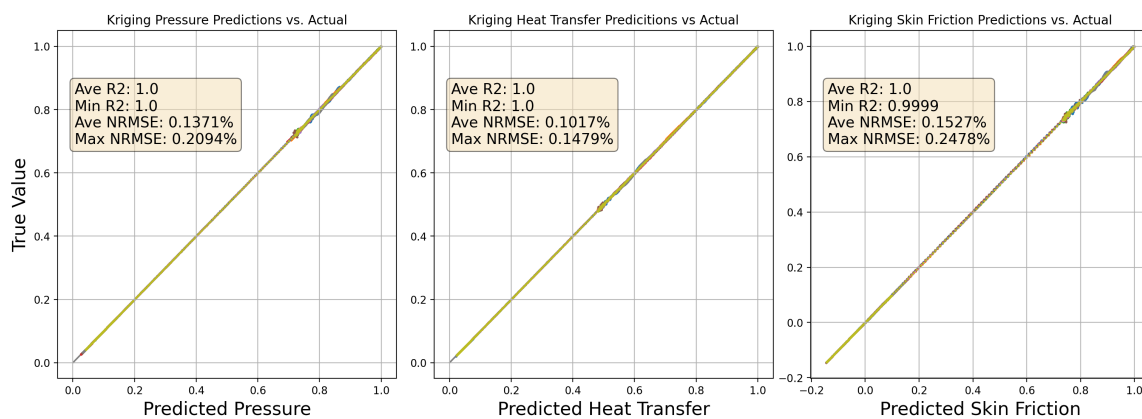

Figure A3. Validation Kriging model metrics for Matern ($\nu = 1.5$) kernel. Each line is a different validation data point.

Sample Kriging predicted profiles of the pressure, heat flux, and skin friction coefficient are shown in Figure A4 for an undeformed cylinder and a mode 2 distortion, $A_1 = 0$, $A_2 = 2$. These types of profiles are generated for the results in Section 3.1, where the peak values of the pressure and heat flux profiles on the flare, the integrated pressure and heat flux over the flare, and the flare corner separation length were recorded and used to generate response surfaces.
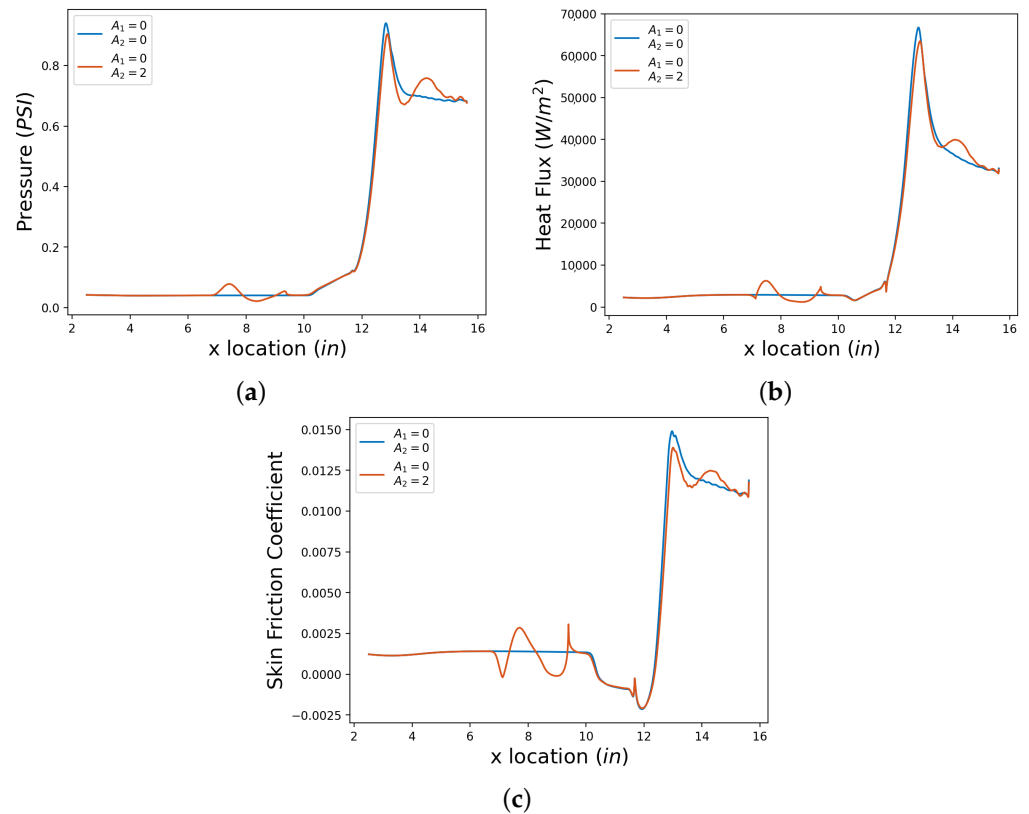

(a)

(b)

(c)

Figure A4. Sample Kriging-predicted profiles—varying amplitude. (**a**) Sample Kriging-predicted pressure profiles. (**b**) Sample Kriging-predicted heat flux profiles. (**c**) Sample Kriging-predicted skin friction coefficient profiles.

Appendix B.2. Surrogate Modeling Generation for Section 3.2

A model incorporating both the modal amplitude and distortion location was also developed. To effectively accommodate the higher dimensional space, an increased number of input sites was selected, resulting in a new Halton sequence of 300 inputs. RANS simulations were conducted at the new input sites with the same fluid inputs described in Section 2. In generating the new surrogate model, the same four kernel architectures were utilized—RBF, Matern, WhiteKernel, and ConstantKernel—and various combinations of them. For brevity, only the top kernel choice, as defined according to the lowest average NRMSE and best average R^2 values, listed in Equation (A4), is shown. In testing the new model, as illustrated in Figure A5, there was a decline in performance due to the addition of a new dimension—a trend consistent with the existing literature [59,73]. The decline was particularly noticeable in skin friction, where the worst-case NRMSE and R^2 values were about 1.5% and 0.9972, respectively. However, the average performance for the output functions remained relatively accurate, with average NRMSE in the order of 0.5% and average R^2 of 0.9998 and 0.9993, noted in Figure A5. Additionally, note the spread of the modeled pressure and heat transfer near the maximum values, as well as the errors near 0 of the skin friction plot. These features indicate relative uncertainty in the peak values of pressure and heat flux, as well as the skin friction near 0, which are among the output functions of interest in this study. Nonetheless, the error metrics for the generated surrogate

model indicate a degree of accuracy that is consistent with findings from similar studies [59] and were sufficient for trend-level analysis. This model was used for the results and discussion in Section 3.2.

$$0.0016 + 2.958 \cdot Matern(lengthscale = 1.44, \nu = 1.5) + WhiteKernel(noiselevel = 0.0187) \quad \text{(A4)}$$
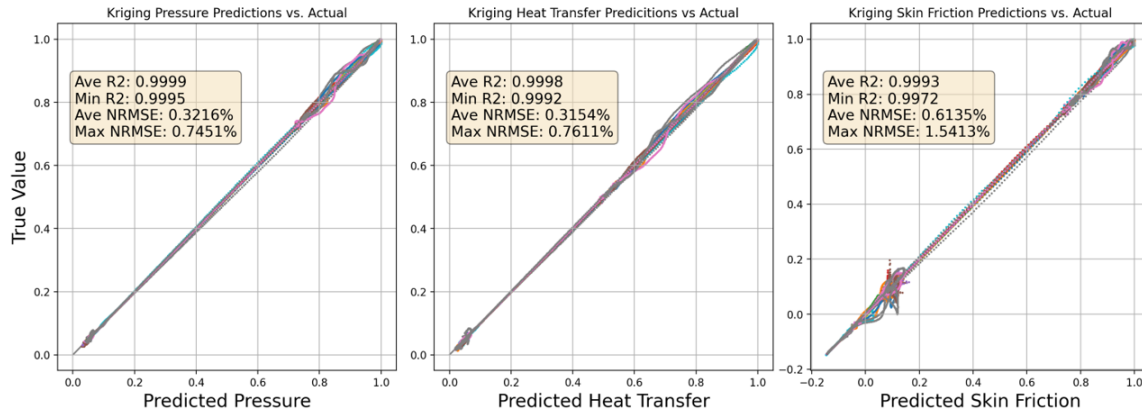

Figure A5. Kriging model metrics for Matern ($\nu = 1.5$) kernel. Each line is a different test data point.

Sample Kriging predicted profiles of the pressure, heat flux, and skin friction coefficient are shown in Figure A6 for an undeformed cylinder and a mode 1 distortion, $A_1 = 2$ and $A_2 = 0$, at $\ell = 2$. This type of profile was generated for the results in Section 3.2, where the peak values of the pressure and heat flux profiles on the flare, the integrated pressure and heat flux over the flare, and the flare corner separation length are recorded and used to generate response surfaces.
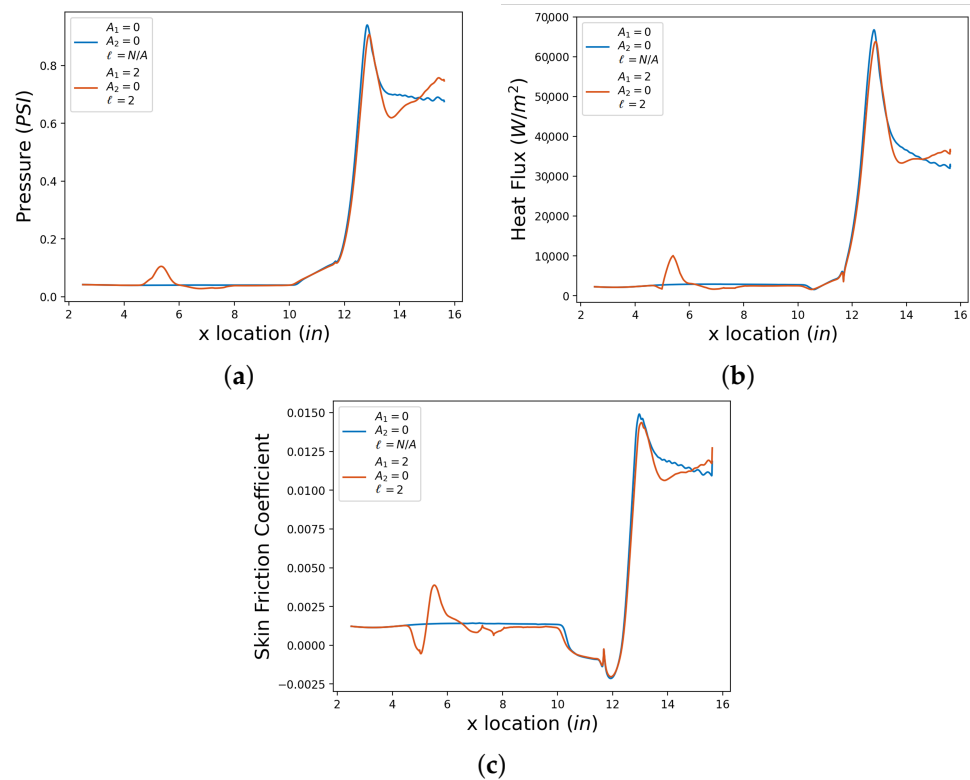

Figure A6. Sample Kriging-predicted profiles—varying location. (**a**) Sample Kriging-predicted pressure profiles. (**b**) Sample Kriging-predicted heat flux profiles. (**c**) Sample Kriging-predicted skin friction coefficient profiles.

References

1. Leyva, I.A. The relentless pursuit of hypersonic flight. *Phys. Today* **2017**, *70*, 30–36. [CrossRef]
2. Schmisseur, J.D. Hypersonics into the 21st century: A perspective on AFOSR-sponsored research in aerothermodynamics. *Prog. Aerosp. Sci.* **2015**, *72*, 3–16. [CrossRef]
3. Eason, T.G.; Spottswood, S. A structures perspective on the challenges associated with analyzing a reusable hypersonic platform. In Proceedings of the 54th AIAA/ASME/ASCE/AHS/ASC Structures, Structural Dynamics, and Materials Conference, Boston, MA, USA, 8–11 April 2013; p. 1747.
4. Spottswood, S.M.; Beberniss, T.J.; Eason, T.G.; Perez, R.A.; Donbar, J.M.; Ehrhardt, D.A.; Riley, Z.B. Exploring the response of a thin, flexible panel to shock-turbulent boundary-layer interactions. *J. Sound Vib.* **2019**, *443*, 74–89. [CrossRef]
5. Beberniss, T.J.; Spottswood, S.M.; Ehrhardt, D.A.; Perez, R. Dynamic response of a thin panel subjected to a shock wave impingement and thermal buckling. In Proceedings of the 33rd AIAA Aerodynamic Measurement Technology and Ground Testing Conference, Denver, CO, USA, 5–9 June 2017. [CrossRef]
6. Peltier, S.J.; Rice, B.E.; Szmodis, J.M.; Ogg, D.R.; Hofferth, J.W.; Sellers, M.E.; Harris, A. Aerodynamic response to a compliant panel in mach 4 flow. In Proceedings of the AIAA Aviation 2019 Forum, Dallas, TX, USA, 17–21 June 2019; p. 3541. [CrossRef]
7. Becks, A.; McNamara, J.; Gaitonde, D. Linking supersonic boundary layer separation to structural deformation using the Kármán–Pohlhausen momentum-integral equation. *Phys. Fluids* **2022**, *34*, 085114. [CrossRef]
8. Shinde, V.; Becks, A.; Deshmukh, R.; McNamara, J.; Gaitonde, D.; Neet, M.; Austin, J. Spatially developing supersonic turbulent boundary layer subjected to static surface deformations. *Eur. J. Mech. B/Fluids* **2021**, *89*, 485–500. [CrossRef]
9. Spottswood, S.M.; Smarslok, B.P.; Perez, R.A.; Beberniss, T.J.; Hagen, B.J.; Riley, Z.B.; Brouwer, K.R.; Ehrhardt, D.A. Supersonic aerothermoelastic experiments of aerospace structures. *AIAA J.* **2021**, *59*, 5029–5048. [CrossRef]
10. Brouwer, K.R.; Perez, R.A.; Beberniss, T.J.; Spottswood, S.M.; Ehrhardt, D.A. Experiments on a thin panel excited by turbulent flow and shock/boundary-layer interactions. *AIAA J.* **2021**, *59*, 2737–2752. [CrossRef]
11. Varigonda, S.; Narayanaswamy, V. Methodology to image the panel surface pressure power spectra in weakly coupled fluid/structure interactions. *Exp. Fluids* **2021**, *62*, 1–17. [CrossRef]
12. Willems, S.; Gülhan, A.; Esser, B. Shock induced fluid-structure interaction on a flexible wall in supersonic turbulent flow. *Prog. Flight Phys.* **2013**, *5*, 285–308.
13. Willems, S.; Gülhan, A.; Steelant, J. Experiments on the effect of laminar–turbulent transition on the SWBLI in H2K at Mach 6. *Exp. Fluids* **2015**, *56*, 49. [CrossRef]
14. Daub, D.; Willems, S.; Gulhan, A. Experiments on the interaction of a fast-moving shock with an elastic panel. *AIAA J.* **2016**, *54*, 670–678. [CrossRef]
15. Currao, G.M.; Neely, A.J.; Kennell, C.M.; Gai, S.L.; Buttsworth, D.R. Hypersonic fluid–structure interaction on a cantilevered plate with shock impingement. *AIAA J.* **2019**, *57*, 4819–4834. [CrossRef]
16. Ostoich, C.; Bodony, D.J.; Geubelle, P.H. Direct numerical simulation of the aeroelastic response of a panel under high speed turbulent boundary layers. In Proceedings of the 43rd Fluid Dynamics Conference, San Diego, CA, USA, 24–27 June 2013. [CrossRef]
17. Ostoich, C.M.; Bodony, D.J.; Geubelle, P.H. Interaction of a Mach 2.25 turbulent boundary layer with a fluttering panel using direct numerical simulation. *Phys. Fluids* **2013**, *25*, 110806. [CrossRef]
18. Sullivan, B.T.; Bodony, D.J.; Whalen, T.; Laurence, S. Direct simulation of fluid–structure interaction in a hypersonic compression-ramp flow. *AIAA J.* **2020**, *58*, 4848–4865. [CrossRef]
19. Whalen, T.J.; Schöneich, A.G.; Laurence, S.J.; Sullivan, B.T.; Bodony, D.J.; Freydin, M.; Dowell, E.H.; Buck, G.M. Hypersonic fluid–structure interactions in compression corner shock-wave/boundary-layer interaction. *AIAA J.* **2020**, *58*, 4090–4105. [CrossRef]
20. Jinks, E.; Bruce, P.; Santer, M. Optimisation of adaptive shock control bumps with structural constraints. *Aerosp. Sci. Technol.* **2018**, *77*, 332–343. [CrossRef]
21. Miller, B.; Crowell, A.; McNamara, J. Modeling and analysis of shock impingements on thermo-mechanically compliant surface panels. In Proceedings of the 53rd AIAA/ASME/ASCE/AHS/ASC Structures, Structural Dynamics and Materials Conference 20th AIAA/ASME/AHS Adaptive Structures Conference 14th AIAA, Honolulu, HI, USA, 23–26 April 2012; p. 1548.
22. Deshmukh, R.; Culler, A.J.; Miller, B.A.; McNamara, J.J. Response of skin panels to combined self-and boundary layer-induced fluctuating pressure. *J. Fluids Struct.* **2015**, *58*, 216–235. [CrossRef]
23. Gogulapati, A.; Deshmukh, R.; Crowell, A.; McNamara, J.; Vyas, V.; Wang, X.; Mignolet, M.; Beberniss, T.; Spottswood, S.; Eason, T. Response of a Panel to Shock Impingement: Modeling and Comparison with Experiments. In Proceedings of the AIAA-2014-0148, National Harbor, MD, USA, 13–17 January 2014.
24. Gogulapati, A.; Deshmukh, R.; McNamara, J.; Vyas, V.; Wang, X.; Mignolet, M.; Beberniss, T.; Spottswood, S.; Eason, T. Response of a Panel to Shock Impingement: Modeling and Comparison with Experiments—Part 2. In Proceedings of the AIAA-2015-0685, Orlando, FL, USA, 5–9 January 2015.
25. Délery, J.; Marvin, J.G.; Reshotko, E. *Shock-Wave Boundary Layer Interactions*; Advisory Group for Aerospace Research & Development: Neuilly-sur-Seine, France, 1986. Available online: https://apps.dtic.mil/sti/pdfs/ADA171302.pdf (accessed on 14 May 2024).

26. Kaushik, M.; Humrutha, G. Review of shock-boundary layer controlled interactions studies in high speed intakes. *J. Aerosp. Eng. Technol.* **2015**, *5*, 1–14.

27. Shinde, V.; McNamara, J.; Gaitonde, D. Control of transitional shock wave boundary layer interaction using structurally constrained surface morphing. *Aerosp. Sci. Technol.* **2020**, *96*, 105545. [CrossRef]

28. Zhou, L.; Chen, D.; Tao, Y.; Liu, G.; Song, S.; Zhong, S. Passive shock wave/boundary layer control of wing at transonic speeds. *THeoretical Appl. Mech. Lett.* **2017**, *7*, 325–330. [CrossRef]

29. Karkoulias, D.G.; Bourdousi, P.V.N.; Margaris, D.P. Passive Control of Boundary Layer on Wing: Numerical and Experimental Study of Two Configurations of Wing Surface Modification in Cruise and Landing Speed. *Computation* **2023**, *11*, 67. [CrossRef]

30. Peltier, S.J.; Brouwer, K.R.; Perez, R.; Spottswood, S.M.; Hammack, S. Boundary-Layer Measurements for FTSI Systems: Influence of Panel Flutter on a Mach 2 Turbulent Boundary-Layer. In Proceedings of the AIAA SCITECH 2023 Forum, National Harbor, MD, USA, 3–27 January 2023; p. 0946.

31. Settles, G.S.; Fitzpatrick, T.J.; Bogdonoff, S.M. Detailed Study of Attached and Separated Compression Corner Flowfields in High Reynolds Number Supersonic Flow. *AIAA J.* **1979**, *17*, 579–585. [CrossRef]

32. Kuntz, D.; Amatucci, V.; Addy, A. Turbulent boundary-layer properties downstream of the shock-wave/boundary-layer interaction. *AIAA J.* **1987**, *25*, 668–675. [CrossRef]

33. Smits, A.J.; Muck, K.C. Experimental study of three shock wave/turbulent boundary layer interactions. *J. Fluid Mech.* **1987**, *182*, 291–314. [CrossRef]

34. Friedlander, D.J. *Understanding the Flow Physics of Shock Boundary-Layer Interactions Using CFD and Numerical Analyses*; University of Cincinnati: Cincinnati, OH, USA, 2013. Available online: https://ntrs.nasa.gov/api/citations/20140003148/downloads/20140003148.pdf (accessed on 14 May 2024).

35. Ardonceau, P.L. The structure of turbulence in a supersonic shock-wave/boundary-layer interaction. *AIAA J.* **1984**, *22*, 1254–1262. [CrossRef]

36. Selig, M.; Andreopoulos, J.; Muck, K.; Dussauge, J.; Smits, A. Turbulence structure in a shock wave/turbulent boundary-layer interaction. *AIAA J.* **1989**, *27*, 862–869. [CrossRef]

37. Bookey, P.; Wyckham, C.; Smits, A.; Martin, P. New experimental data of STBLI at DNS/LES accessible Reynolds numbers. In Proceedings of the 43rd AIAA Aerospace Sciences Meeting and Exhibit, Reno, NV, USA, 10–13 January 2005; p. 309.

38. Wu, M.; Taylor, E.M.; Martín, M.P. Assessment of STBLI DNS data and comparison against experiments. In Proceedings of the 35th AIAA Fluid Dynamics Conference and Exhibit, Toronto, ON Canada, 6–9 June 2005. [CrossRef]

39. Wu, M.; Martin, M.P. Direct numerical simulation of supersonic turbulent boundary layer over a compression ramp. *AIAA J.* **2007**, *45*, 879–889. [CrossRef]

40. Pham, H.T.; Gianikos, Z.N.; Narayanaswamy, V. Compression ramp induced shock-wave/turbulent boundary-layer interactions on a compliant material. *AIAA J.* **2018**, *56*, 2925–2929. [CrossRef]

41. Eitner, M.A. Experimental Investigation of Fluid-Structure Interaction of a Compliant Panel under a Mach 2 Compression Ramp Shock-Boundary Layer Interaction. Ph.D. Thesis, The University of Texas at Austin, Austin, TX, USA, 2021.

42. Chism, J.R. Experimental Investigation of the Downstream Effects from High-Speed Fluid Structure Interactions and the Development of Supporting Diagnostics. Ph.D. Thesis, The University of Tennessee, Knoxville, TN, USA, 2023.

43. Chism, J.R.; Kreth, P.A.; Schmisseur, J.D. Characterization of Downstream Effects from a WavyWall on a Hollow Cylinder at Mach 4. In Proceedings of the AIAA SCITECH 2023 Forum, National Harbor, MD, USA, 23-27 January 2023. [CrossRef]

44. Stookesberry, D. An Industry Assessment of HPCMP CREATE-AV Kestrel. In Proceedings of the 53rd AIAA Aerospace Sciences Meeting, Kissimmee, FL, USA, 5–9 January 2015; p. 0552.

45. Morton, S.A.; Tillman, B.; McDaniel, D.R.; Sears, D.R.; Tuckey, T.R. Kestrel–A Fixed Wing Virtual Aircraft Product of the CREATE Program. In Proceedings of the 2009 DoD High Performance Computing Modernization Program Users Group Conference, San Diego, CA, USA, 15–18 June 2009; pp. 148–152. [CrossRef]

46. McDaniel, D.R.; Tuckey, T.; Morton, S.A. The HPCMP CREATE^TM-AV Kestrel Computational Environment and its Relation to NASA's CFD Vision 2030. In Proceedings of the 55th AIAA Aerospace Sciences Meeting, Grapevine, TX, USA, 9–13 January 2017. [CrossRef]

47. Potter, D.; Eymann, T.A. CFD Based Reduced Order Modeling for Hypersonic Vehicles Using CREATE(TM)-AV Kestrel. In Proceedings of the AIAA Aviation 2019 Forum, Dallas, TX, USA, 17–21 June 2019. [CrossRef]

48. Gragston, M.; Davenport, K.; Siddiqui, F.; Webber, N.; Smith, C.D.; Kreth, P.A.; Schmisseur, J.D. Design and Initial Characterization of the UTSI Mach 7 Ludwieg Tube. In Proceedings of the AIAA SCITECH 2023 Forum, National Harbor, MD, USA, 23–27 January 2023; p. 1457.

49. Forrester, A.; Sobester, A.; Keane, A. *Engineering Design via Surrogate Modeling: A Practical Guide*; John Wiley & Sons: New York, NY, USA, 2008.

50. Queipo, N.V.; Haftka, R.T.; Shyy, W.; Goel, T.; Vaidyanathan, R.; Tucker, P.K. Surrogate-Based Analysis and Optimization. *Prog. Aerosp. Sci.* **2005**, *41*, 1–28. [CrossRef]

51. Brouwer, K.R.; McNamara, J.J.; Chen, J.P.; Mazumder, S.; Smarslok, B.P. *Enhancement of CFD Surrogate Approaches for Thermo-Structural Response Prediction in High-Speed Flows*; Ohio State University, Columbus, OH, USA, 2023. Available online: https://etd.ohiolink.edu/acprod/odb_etd/ws/send_file/send?accession=osu1543340520905498&disposition=inline (accessed on 14 May 2024).

52. Skujins, T.; Cesnik, C. Reduced-Order Modeling of Unsteady Aerodynamics Across Multiple Mach Regimes. *J. Aircr.* **2014**, *51*, 1681–1704. [CrossRef]
53. Crowell, A.R.; McNamara, J.J.; Miller, B.A. Hypersonic Aerothermoelastic Response Prediction of Skin Panels Using Computational Fluid Dynamic Surrogates. *J. Aeroelast. Struct. Dyn.* **2011**, *2*, 3–30.
54. Dreyer, E.R.; Klock, R.; Grier, B.J.; McNamara, J.J.; Cesnik, C.E. Multi-Discipline Modeling of Complete Hypersonic Vehicles Using CFD Surrogates. In Proceedings of the 58th AIAA/ASCE/AHS/ASC Structures, Structural Dynamics, and Materials Conference, Grapevine, TX, USA, 9–13 January 2017.
55. Falkiewicz, N.; Cesnik, C.E.S.; Crowell, A.R.; McNamara, J.J. Reduced-Order Aerothermoelastic Framework for Hypersonic Vehicle Control Simulation. *AIAA J.* **2011**, *49*, 1625–1646. [CrossRef]
56. VanderWyst, A.S.; Shelton, A.B.; Martin, C.L.; Neergaard, L.J.; Witeof, Z.D. Reduced Order Models for Generation of Large, High Speed Aerodynamic Databases with Jet Interactions. In Proceedings of the 57th AIAA/ASCE/AHS/ASC Structures, Structural Dynamics, and Materials Conference, San Diego, CA, USA, 4–8 January 2016.
57. Gogulapati, A.; Brouwer, K.R.; Wang, X.Q.; Murthy, R.; McNamara, J.J.; Mignolet, M.P. Full and Reduced Order Aerothermoelastic Modeling of Built-Up Aerospace Panels in High-Speed Flows. In Proceedings of the 58th AIAA/ASCE/AHS/ASC Structures, Structural Dynamics, and Materials Conference, Grapevine, TX, USA, 9–13 January 2017.
58. Wang, C.; Duan, Q.; Gong, W.; Ye, A.; Di, Z.; Miao, C. An evaluation of adaptive surrogate modeling based optimization with two benchmark problems. *Environ. Model. Softw.* **2014**, *60*, 167–179. [CrossRef]
59. Korenyi-Both, B.T.E.; McNamara, J.; Reasor, A.A.D.; Srinivasan, J.M. Assessment of Multi-Fidelity Surrogate Methods for Expedient Loads Prediction in High-Speed Flows. Available online: https://etd.ohiolink.edu/acprod/odb_etd/ws/send_file/send?accession=osu1679258588528361&disposition=inline (accessed on 14 May 2024).
60. Kucherenko, S.; Albrecht, D.; Saltelli, A. Exploring multi-dimensional spaces: A comparison of Latin hypercube and quasi Monte Carlo sampling techniques. *arXiv* **2015**, arXiv:1505.02350.
61. Virtanen, P.; Gommers, R.; Oliphant, T.; Haberland, M.; Reddy, T.; Cournapeau, D.; Burovski, E.; Peterson, P.; Weckesser, W.; Bright, J.; et al. SciPy 1.0: fundamental algorithms for scientific computing in Python. *Nat. Methods* **2020**, *17*, 261–272. [CrossRef]
62. Grier, B.J.; Brouwer, K.R.; Dreyer, E.R.; McNamara, J.J. Controlling the p-norm function space distribution of linked surrogate parameters. *AIAA J.* **2019**, *57*, 2659–2662. [CrossRef]
63. Krige, D.G. A statistical approach to some basic mine valuation problems on the Witwatersrand. *J. South. Afr. Inst. Min. Metall.* **1951**, *52*, 119–139.
64. Matheron, G. Principles of geostatistics. *Econ. Geol.* **1963**, *58*, 1246–1266. [CrossRef]
65. Rasmussen, C.E.; Williams, C.K.I. *Gaussian Processes for Machine Learning*; MIT Press: Cambridge, MA, USA, 2006.
66. Pedregosa, F.; Varoquaux, G.; Gramfort, A.; Michel, V.; Thirion, B.; Grisel, O.; Blondel, M.; Prettenhofer, P.; Weiss, R.; Dubourg, V.; et al. Scikit-learn: Machine Learning in Python. *J. Mach. Learn. Res.* **2011**, *12*, 2825–2830.
67. Duvenaud, D. Automatic Model Construction with Gaussian Processes. Ph.D. Thesis, University of Cambridge, Cambridge, UK, 2014.
68. Brouwer, K.R.; Gogulapati, A.; McNamara, J.J. Interplay of Surface Deformation and Shock-Induced Separation in Shock/Boundary-Layer Interactions. *AIAA J.* **2017**, *55*, 4258–4273. [CrossRef]
69. Gramola, M.; Bruce, P.J.; Santer, M. Experimental FSI study of adaptive shock control bumps. *J. Fluids Struct.* **2018**, *81*, 361–377. [CrossRef]
70. Bruce, P.; Colliss, S. Review of research into shock control bumps. *Shock Waves* **2015**, *25*, 451–471. [CrossRef]
71. Mayer, R.; Lutz, T.; Krämer, E.; Dandois, J. Control of transonic buffet by shock control bumps on wing-body configuration. *J. Aircr.* **2019**, *56*, 556–568. [CrossRef]
72. John, A.; Qin, N.; Shahpar, S. Using shock control bumps to improve transonic fan/compressor blade performance. *J. Turbomach.* **2019**, *141*, 081003. [CrossRef]
73. Meng, X.; Karniadakis, G.E. A composite neural network that learns from multi-fidelity data: Application to function approximation and inverse PDE problems. *J. Comput. Phys.* **2020**, *401*, 109020. [CrossRef]